2-9-2010

Templated growth of platinum nanostructures

Robert Garcia

Robert Mario Garcia
Candidate

Chemical and Nuclear Engineering
Department

This thesis is approved, and it is acceptable in quality and form for publication:

Approved by the Thesis Committee:

, Chairperson

TEMPLATED GROWTH OF PLATINUM NANOSTRUCTURES

BY

ROBERT M. GARCIA

B.S., CHEMISTRY, UNIVERSITY OF NEW MEXICO, 2007

THESIS

Submitted in Partial Fulfillment of the
Requirements for the Degree of

Master of Science

Chemical Engineering

The University of New Mexico
Albuquerque, New Mexico

December, 2009

ACKNOWLEDGMENTS

I heartily acknowledge Dr. C. Jeffrey Brinker, my co-advisor and thesis chair for all of his support through the years.

I also thank my committee members, Dr. Frank Van Swol, Dr. Yujiang Song, Dr. John Shelnutt, and Dr. Tim Ward, for their valuable recommendations pertaining to this study and assistance in my professional development. Gratitude is extended to the University of New Mexico Center for Micro-engineered Materials and Sandia National Laboratories for the funding to pursue this research.

To my editor and mentor, Dr. Song, though a small word of thanks is not enough for many months work, I do thank you from the bottom of my heart.

To my family, friends and co-workers, who gave me immeasurable support over the years. Your encouragement is greatly appreciated.

TEMPLATED GROWTH OF PLATINUM NANOSTRUCTURES

BY

ROBERT M. GARCIA

ABSTRACT OF THESIS

Submitted in Partial Fulfillment of the
Requirements for the Degree of

MASTER OF SCIENCE
CHEMICAL ENGINEERING

The University of New Mexico
Albuquerque, New Mexico

December, 2009

TEMPLATED GROWTH OF PLATINUM NANOSTRUCTURES

by

Robert M. Garcia

B.S., Chemistry, University of New Mexico, 2007

ABSTRACT

Novel platinum nanostructures were synthesized by templating the growth of platinum on treated polymer surfaces and within disk-like aqueous bicellar assemblies. The growth mechanisms of all structures were examined in detail.

Platinum hollow nanospheres with uniform shell thickness were prepared by the seeded growth of platinum on the surface of latex beads with an adsorbed porphyrin photocatalyst followed by core removal.

Templating bicelles of a high yield were synthesized for the first time and verified by electron microscopy. Dendritic platinum nanowheels were obtained as a result of confined growth within the bicellar interior. Sintering experiments revealed an unusual stability of the nanowheels prompting further examination of their catalytic properties. The nanowheels have similar catalytic performance to a commercial catalyst but provide an improvement in stability.

These platinum nanostructures have advantages over bulk catalyst as a result of improved surface to volume ratios leading to reduced costs in catalytic applications.

TABLE OF CONTENTS

LIST OF FIGURES

Chapter 1

Introduction

Many applications require the use of rare and precious metal catalyst. In most cases these metals are available in extremely limited quantities and are thus very expensive. The advent of nanochemistry and nanoengineering has created a new pathway in which the required amount of precious metals can be minimized while simultaneously increasing the catalytic activity and material usage efficiency. Manipulation of the structural morphology at the nanometer scale by the use of both templated and non-templated growth mechanisms has led to the synthesis of varied shapes and sizes of structures with greatly improved surface to volume ratios and unique size-related properties when compared with their bulk material counterparts. This thesis explores two novel techniques for the engineered synthesis of metallic nanostructures including the development of hollow platinum nanospheres using a hard template of commercially available latex spheres, and dendritic platinum nanowheels using a soft template of aqueous bicelles. Platinum was chosen as the metal of interest for these experiments as it is one of the most widely used and important catalytic metals used today.

The Problem with Precious Metal Catalysts

Platinum is one of the most common catalysts and is used in many chemical reactions. It is used as an electrocatalyst in proton exchange membrane fuel cells[1,2], as a catalyst in solar water splitting devices[3,4], and as a common redox catalyst. Platinum is available in extremely limited supply and is thereby very expensive. Other metals such as palladium share a similar fate. Continued use of these precious metals in emerging technologies will require efficient usage economy and cost minimization in order to feasibly

implement them into widespread commercial application within emerging technologies. Nanostructuring can significantly reduce this problem by taking advantage of novel size related improvements in catalytic activity.

Nanostructuring to Improve Catalyst Efficiency and Reduce Costs

Developments in the field of nanoscience have opened up new pathways by which it may be possible to reduce both the cost and required amount of catalytic materials necessary for chemical processes by controlling the formation of structural features at the nanoscale level. In addition, nanostructured materials have also been shown to have greatly improved surface to volume ratios and catalytic activities over their bulk material counterparts. Size, shape and surface area all play a vital role in the catalytic activity of precious metal catalysts[5]. A diverse set of techniques have been developed in recent years which allow for the tuning and control of these parameters. At the base level two approaches exist, the top-down approach which introduces nanoscale features by means of the alteration of macroscale bulk materials usually by using state of the art lithographic techniques and the bottom-up approach in which nanoscale features are engineered at the molecular level by careful selection of the synthetic conditions. This report will focus on a bottom-up approach, specifically self-assembly and directed assembly. The concept of self-assembly arises from electrostatic, hydrophobic/hydrophilic, π-π interactions, and hydrogen bonding which result in the reorganization of a disordered system of molecules into an ordered assembly to reach a stable state. Directed assembly relies on externally induced conditions such as electromagnetism and photoexcitation among others in order to align and/or direct the formation of nanostructures. In taking advantage of these fundamental processes a great number of nanostructured materials such as nanospheres[6-

[8], nanowires[9,10], and nanotubes[11] have been synthesized and have shown vast improvements in catalytic efficiency when applied to the synthesis of metallic structures.

Templated Growth of Metallic Nanostructures

Metallic nanostructures have been synthesized by various methods including templated and non-templated routes. Some non-templated approaches include epitaxial growth using chemical vapor deposition (CVD)[12], and top-down approaches such as nanoscale patterning of photoresists using focused ion beam and electron beam nanolithography[13,14]. While these techniques do have merit and can provide a high level of order within the structures, they require expensive instrumentation and difficult synthetic schemes. In addition lithographic methods are restricted in feature size due the physical limitations of optical diffraction. In contrast, using a bottom-up approach growth mechanisms such as hard and soft templating offer relatively simple and cost effective wet chemistry syntheses. Typically, the simplicity gained in using the bottom-up approach is counteracted by a loss in overall order and uniformity, thus requiring very careful choice of reactants and materials to achieve good results. Previously, nanoscale metal shells have been prepared by metal deposition onto a central templating core followed by core removal[15-19] and co-assembly of metal nanoparticles with organic molecules[20]. More recently our research group has developed a number of hard and soft template based synthetic strategies. Some examples of our soft templating strategies are the use of spherical liposomes in conjunction with photocatalytic seeding to form hollow platinum nanocages[21], the use of a reverse micelle system to form platinum nanowire networks[10], and surfactant bicelles to form platinum nanowheels[22] which partially form as the subject of this thesis. In the realm of hard templates we have utilized

commercially available silica to form platinum core shell structures[8] and latex beads as templates for the photocatalytically seeded growth of platinum on the surface, followed by core removal to form porous hollow platinum nanospheres[6] which were developed as part of this thesis project.

Chapter 2

Review of Related Literature

Self Assembly

The process of self assembly can be described as the spontaneous organization of materials without an external driving force, specifically through non-covalent interactions such as Van der Waals, electrostatic, hydrogen bonding, and π-π interactions[23]. Typically, this process involves asymmetric molecules that are predisposed to form well defined supramolecular structures[23]. A basic example of this process is the hydrophobically driven self-assembly of amphiphillic surfactants above the critical micelle concentration (CMC) to form molecular micelles in a polar medium. Amphiphillic molecules are a class of compounds that contain both a polar-head group and non-polar tail. Below the CMC these molecules do not form supramolecular structures due to the sparsity of neighboring molecules with which to combine thus leaving exposed non-polar segments in contact with polar solvent molecules resulting in a disordered state. When the CMC is reached these molecules combine and align into micelles and thus reduce contact between non-polar and polar groups which also leads to an overall reduction in free energy of the system. A prime example of this phenomenon occurs when the polar head groups of the common surfactant cetyltrimethylammonium bromide (CTAB) align toward the exterior surface while the non-polar tail groups are shifted toward the interior space when dissolved in a polar medium as shown in figure 1c. The structural mesophases present in a system are also concentration dependent and can be tuned to form spherical micelles, hexagonal, cubic, and lamellar structures as shown in the ternary phase diagram of CTAB in figure 2[23]. Systems of inverse structures are also

possible by using non-polar organic solvents and mixtures of polar/non-polar solvents. Evaporation induced self assembly (EISA) is a simple extension of the concept of self assembly in which the formation of supramolecular structures is driven by the evaporation of a solvent or co-solvent in systems of materials with concentration dependent organizational properties[23]. EISA can be used to direct the nucleation of materials onto a specific surface or interface as a result of changes in the solubility of materials with the evolving increase in concentration. In chapter 3 of this report a process will be described in which a hydrophobic tin porphyrin photocatalyst will be deposited onto the hydrophobic surface of latex beads by EISA which allows for the novel photocatalytic seeding of platinum directly onto the surface of the latex beads to form core-shell structures. As a soft template disk-like bicelles, a relative of micelles, containing mixed short/long chain lipids/detergents will also be utilized in the formation of dendritic platinum nanowheels by nucleation of platinum within the hydrophobic interior of the bicelles. The formation of the bicelle template is another example of the hydrophobically driven self-assembly of amphiphillic molecules analogous to the formation of micelles but with a two component molecular assembly.

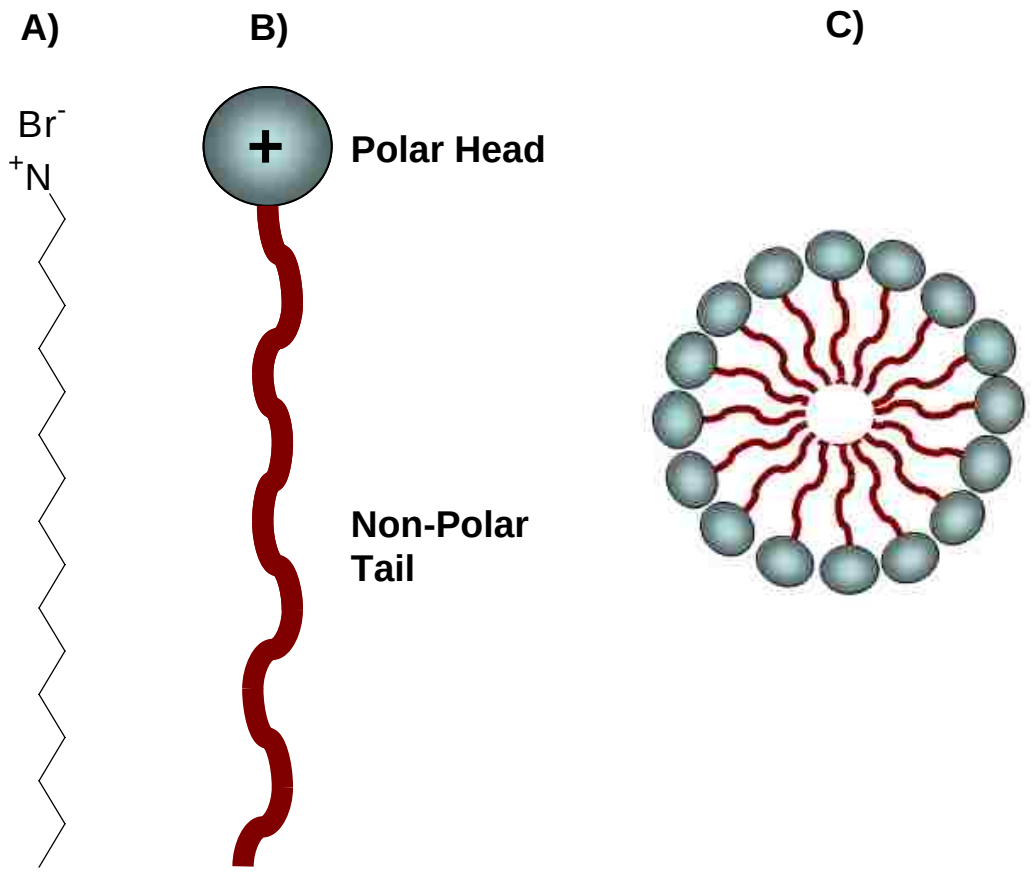

Figure 1: CTAB A) chemical structure, B) ball and stick diagram, C) spherical micelle assembly isolating the non-polar tails within the interior region.

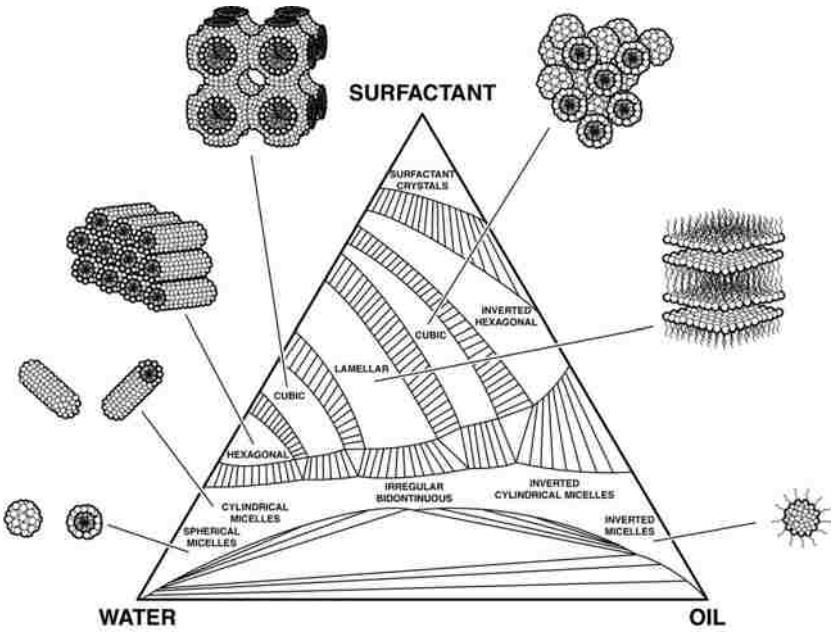

Figure 2: Ternary phase diagram for CTAB describing the many possible mesophases achievable by manipulation of the concentration of surfactant, water, and oil (reprinted with permission of the author)[23].

Sn Porphyrin Photocatalysis

In this report a photocatalytic seeding strategy will be utilized to initiate the nucleation of large numbers of small platinum seeds on the hydrophobic surface of latex beads. Sn (IV) octaethylporphyrin dichloride (SnOEP) shown in figure 3 was chosen in light of its hydrophobicity and the fact that SnOEP can easily form excited porphyrin radicals when subjected to a white tungsten light source in the presence of an electron donor. This strategy is easily extended to numerous reaction conditions by careful selection of the tin porphyrin in order to achieve the desired properties.

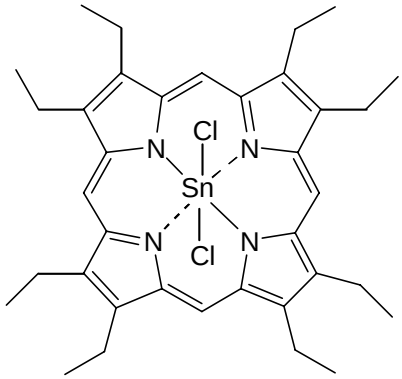

Figure 3: Sn(IV)Octaethylporphyrin Dichloride

Based on previous research large numbers of platinum seeds can be rapidly generated using Sn porphyrin photocatalysis according to the following simplified reactions[6,8,21].

$$SnOEP + h\nu \rightarrow SnOEP^* \qquad (1)$$

$$SnOEP^* + ED \rightarrow [SnOEP]^{-*} + ED_{ox} \qquad (2)$$

$$2[SnOEP]^{-*} + Pt^{2+} \rightarrow 2SnOEP + Pt^0 \qquad (3)$$

In the first step the tin porphryin is subjected to a white tungsten light source creating a tin porphyrin excited state. Next the exited porphyrin reacts with an electron donor to form a highly reactive porphyrin radical anion and the oxidized form of the electron

donor. In the final step two porphyrin radical anions react with the platinum (II) complex, regenerating the SnOEP catalyst and yielding zero-valent platinum metal. Once the platinum seeds achieve a certain size they can become autocatalytic aiding in the further reduction of any remaining platinum complex until exhaustion[21]. This photocatalytic seeding strategy can be combined with hard and soft templating methods in the development of new porous and dendritic platinum nanostructures with potential applications in the catalysis industry.

Conclusion

By taking advantage of the principles of self assembly and porphyrin photocatalysis it is possible to create novel hard and soft templated reaction schemes to build platinum nanomaterials with beneficial dendritic features that also offer a simple wet chemistry alternative to more complex top down approaches while still retaining a level of order in the system. This thesis will explore these principles in the development of dendritic platinum hollow nanospheres and dendritic platinum nanowheels. Hard templating in conjunction with porphyrin photocatalytic seeding will be used to synthesize the platinum hollow spheres while self assembly of a soft bicelle template in conjunction with hydrophobic/hydrophilic interaction of a platinum complex will be used in the synthesis of the platinum nanowheels. These novel nanostructures have a high potential to reduce the cost and provide adequate catalytic activity for platinum and other metal catalysts while reducing the material cost and increasing usage efficiency. These materials have potential applications in the fuel cell industry among many other systems which require precious metal catalysts.

Chapter 3

Light-driven synthesis of hollow platinum nanospheres

(Originally Published in Chemical Communications, 2008)

Hollow nanospheres possess tunable structural features such as shell thickness, interior cavity size, and chemical composition, leading to relatively high surface area, low density, material economy, and reduced cost compared with their solid counterparts[24]. Metallic hollow nanospheres are of special interest and importance due to various applications in biomedical[24-26], catalytic[27], and optical sciences[28]. Previously, nanoscale metal shells have been prepared by metal deposition onto a central core followed by core removal[15-19], and co-assembly of metal nanoparticles with organic molecules[20]. Using unilamellar liposomes to confine the growth of metallic nanosheets within a liposomal bilayer, we recently used a tin(IV) porphyrin photocatalyst to control the sheet size to prepare spherical nanocages[7]. We now report a new method of preparing Pt nanospheres that utilizes polystyrene beads covered with a porphyrin photocatalyst to grow uniform and porous platinum nanoshells. Subsequent removal of the polystyrene core with an organic solvent results in hollow platinum nanospheres. Synthetic control over the nanoshell is realized by simply varying the concentration of platinum precursor at fixed light exposure. Fig. 4 illustrates the synthetic scheme for the preparation of platinum hollow spheres, including evaporation induced self assembly of hydrophobic tin(IV) octaethylporphyrin (SnOEP, Frontier Scientific) on hydrophobic polystyrene beads (Bangs Laboratories), irradiation with visible light to promote photocatalytic seeding, autocatalytic growth of seeds to form a platinum shell, and dissolution of the beads and SnOEP. The key to the synthesis is the generation of a large number of initial platinum

seeds in the vicinity of the SnOEP molecules on each bead. When the seeds reach a critical size (about 2 nm), they become catalytic and autocatalyze the further reduction of platinum complex and growth of the seeds into dendrites until the Pt complex is completely consumed[29,30]. Consequently, many neighboring small dendrites join to evenly cover the beads and form the spherical platinum nanoshells.

Experimental Section

In a typical synthesis, 1 mL aqueous suspension of beads with an average diameter of 99 nm (10.2 wt% solid content) is mixed with 9 mL of ethanol containing 17.6 mg SnOEP in a round-bottom flask. Subsequently, ethanol and water in the mixture are removed by rotary evaporation resulting in pink flakes that peel off the glass wall. The flakes of polystyrene beads with adsorbed SnOEP are collected and further dried overnight in a desiccator under vacuum. Because SnOEP molecules are hydrophobic, they are expected to adsorb onto the hydrophobic surface of the beads. 1.76 mL of 20 mM aged K_2PtCl_4 aqueous solution and 0.24 mL water from a Barnstead Nanopure system (Chesterland, OH) are mixed with 2 mg of the dried beads coated with SnOEP. The mixture is sonicated for an hour in a water-bath cleaner to well suspend the beads. Next, 2 mL of 150 mM ascorbic acid (AA) aqueous solution is added to the above mixture. A representative UV–visible spectrum (Fig. 5, spectrum a) of the initial reaction system ($[K_2PtCl_4]$ = 8.8 mM, [AA] = 75 mM, ~6.2×10^{12} beads mL^{-1}, [SnOEP] = ~10.4 μM) shows a characteristic absorption peak at 402 nm for SnOEP molecules. The high sloping baseline reflects light scattering caused by the presence of the colloidal beads. The weaker absorption features of the Pt complex in spectrum a can be identified with the aid of the spectrum b (Fig. 5) of the pure aqueous Pt complex (8.8 mM). The reaction

system reacts under stirring and irradiation by two incandescent light sources (800 nmol cm^2 s^{-1}) for 30 minutes. After discontinuation of the stirring, a colorless transparent supernatant with a black precipitate at the bottom is observed, suggesting that the reduction reaction has gone to completion and the beads have settled out.

Results and Discussion

The UV–visible spectrum of the supernatant obtained is shown in spectrum c of Fig. 5; it shows that the absorption peaks (and the light scattering) disappear after the reaction and confirms that the reduction reaction is complete.

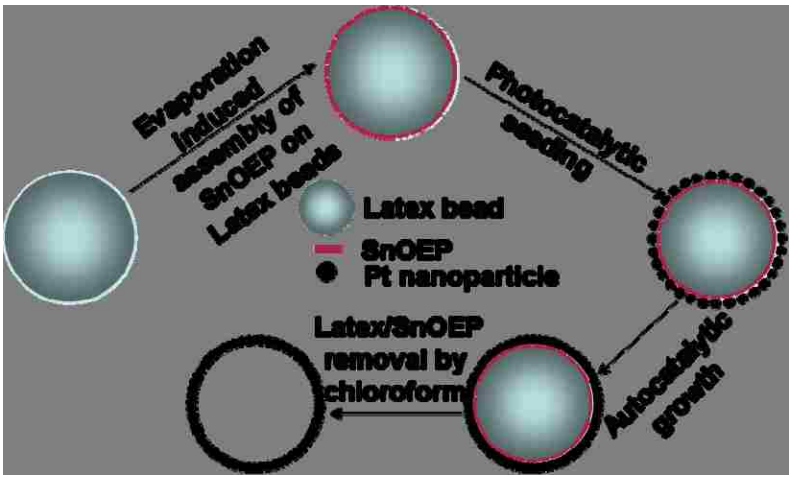

Figure 4: Diagram of steps for the synthesis of hollow platinum nanospheres.

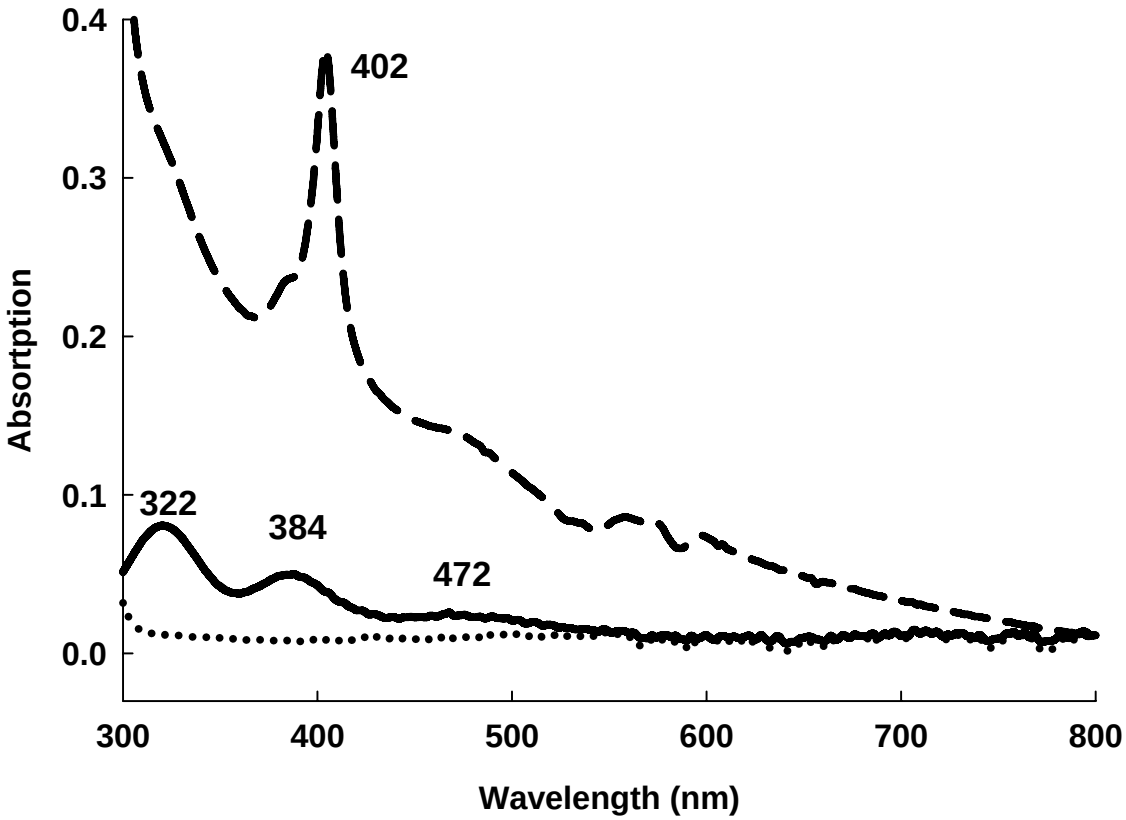

Figure 5: UV–vis spectrum of a typical reaction system before (dashed) and after reaction (dotted). To identify the absorption maxima of the platinum complexes, a characteristic UV–vis spectrum of aqueous platinum salt is included (solid).

The SnOEP-modified beads precipitate out likely as a result of the heavy platinum coating. Transmission electron microscopy (TEM) of the black precipitate reveals that platinum shells with polystyrene cores are obtained as shown in Fig. 6a. The platinum core-shell nanostructures have a uniform shell thickness of 12.4 ± 1.8 nm based on the measurement of 100 individual shells in different areas (Fig. 6b). The monodispersity of the nanoshell thickness arises from the photocatalytic seeding process, which rapidly generates a large number of initial seeds on each bead according to the simplified reactions:

$$\mathrm{SnOEP} + h\nu \rightarrow \mathrm{SnOEP}^* \qquad (1)$$

$$\mathrm{SnOEP}^* + \mathrm{ED} \rightarrow [\mathrm{SnOEP}]^{-*} + \mathrm{ED}_{ox} \qquad (2)$$

$$2[\mathrm{SnOEP}]^{-*} + \mathrm{Pt}^{2+} \rightarrow 2\mathrm{SnOEP} + \mathrm{Pt}^0 \qquad (3)$$

where AA is used as the electron donor (ED) and Pt^{2+} is provided by aged aqueous platinum salt (K_2PtCl_4). The platinum seeds are primarily produced in the first 2–3 minutes of irradiation by photocatalysis. During this initial period of seed formation, the contribution of the direct chemical reduction of the Pt complex by AA is negligible[30,31]. Afterwards, the reaction mixture turns black, shutting down the photocatalytic seeding process since there is not enough light available to drive significant photocatalytic reduction. The seeds produced in the initial period then grow autocatalytically for almost the same length of time and thus achieve similar final sizes. The nanoshells are formed by the joining of these complex-shaped particles, which appear to be dendrites[30,31] (Fig. 6a and e); consequently, the shells are porous due to incomplete platinum coverage of dendrites on the beads. The central polystyrene core and adsorbed SnOEP can be readily dissolved away by placing the dried samples into chloroform for at least 5 minutes under

ambient conditions. Most of the platinum nanoshells are intact after chloroform treatment as shown in Fig. 6c, suggesting that the platinum shells are well formed even for this porous structure. Even more convincingly, the TEM images in Fig. 6 a and c shows that the thickness of the platinum shells is uniform from shell to shell owing partly to the enhanced contrast of high-angle annular dark-field (HAADF) scanning TEM[32]. A scanning electron microscopy (SEM) image (Fig. 6d) confirms the structural integrity of platinum nanoshells after central core removal. The inset of the SEM image shows an atypical region with several broken platinum nanospheres, demonstrating that the shell interiors are hollow and that central core removal by chloroform is effective. The presence of nanopores in the platinum shells likely facilitates the removal of the chloroform-dissolved polystyrene and SnOEP.

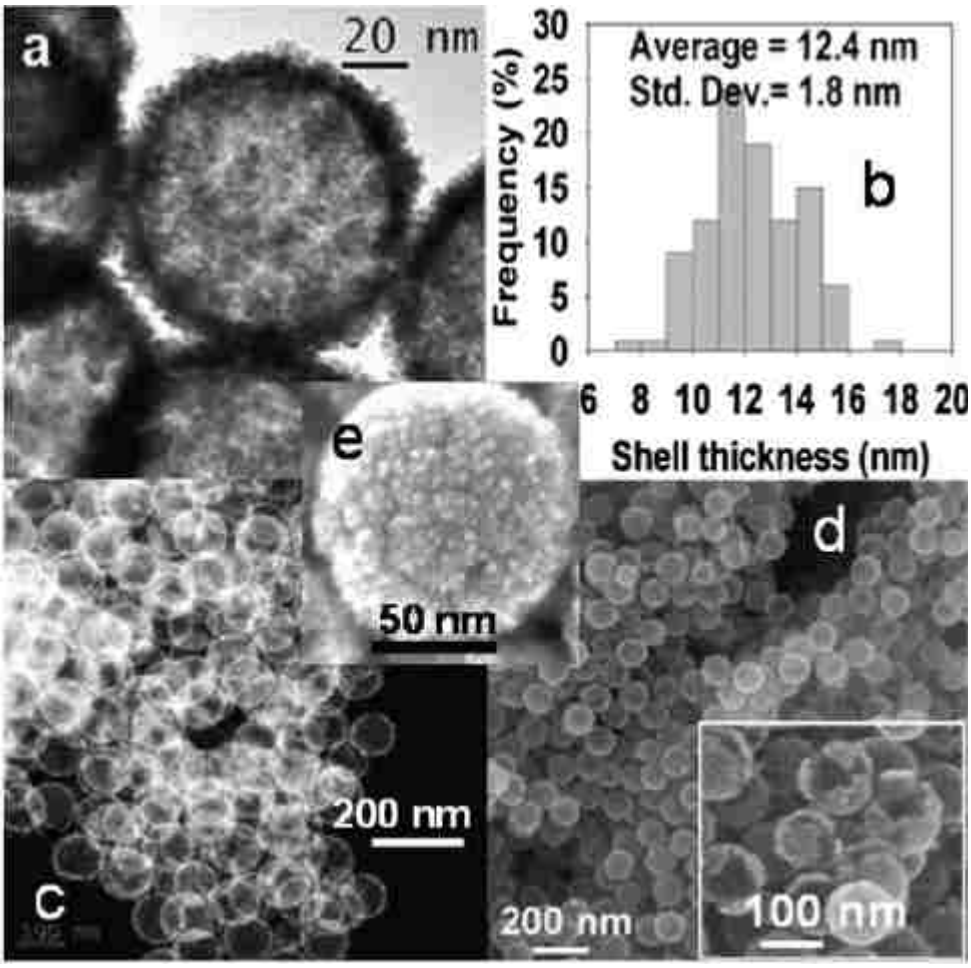

Figure 6: (a) Bright-field TEM image of platinum nanoshells coated on polystyrene beads; (b) Plot of frequency versus thickness for 100 randomly selected sections of platinum nanoshells with average size and standard deviation given in the plot; (c) HAADF scanning TEM image of hollow platinum nanospheres after chloroform treatment; (d) and (e) SEM images of hollow platinum nanospheres at different magnifications after chloroform etching. (Inset: SEM image of several partially broken spheres with hollow interior).

To demonstrate the importance of the photocatalytic seeding for successful preparation of hollow platinum nanospheres, a control experiment was performed in the absence of SnOEP, while holding all the other reaction parameters constant ($[K_2PtCl_4]$ = 8.8 mM, [AA] = 75 mM, ~6.2×10^{12} beads mL^{-1}). Unlike the SnOEP-decorated beads, the reaction system begins to turn black after 25 minutes of irradiation. TEM analysis (Fig. 7) reveals that all the platinum metal has grown onto polystyrene beads, but the platinum nanostructures range widely in size from 3 to 50 nm in diameter. The reason for the poor coverage of the beads is that in the absence of SnOEP and/or light only chemical reduction of the Pt complex by AA occurs. This only provides a relatively small number of seeds, producing relatively large Pt dendrites. Moreover, the dark seeding process is slow and continuous[30], giving a broad distribution of dendrite sizes. That is, compared with photocatalytically formed seeds that are produced in a short initial time interval, seeds produced chemically at different times have varied growth periods leading to a final broad size distribution. In addition, because of the small number of seeds produce chemically, the dendrites, although larger (up to 50 nm), do not adequately bridge to adjacent dendrites to form complete shells. A similar result is obtained in an experiment using SnOEP decorated beads but without light irradiation, giving TEM images (not shown) like those shown in Fig. 7.

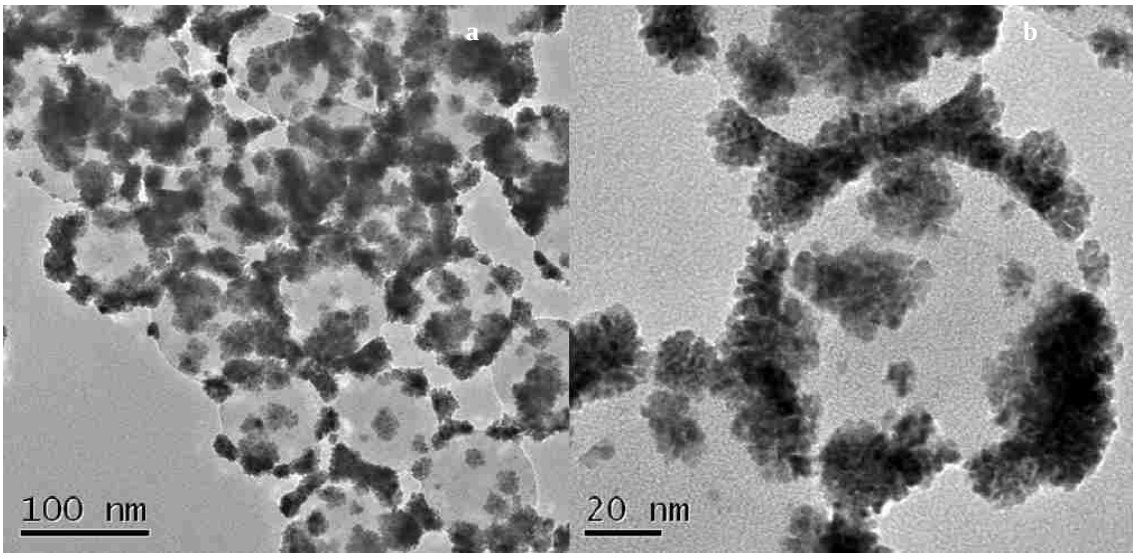

Figure 7 TEM images of Pt nanostructures grown on polystyrene beads without SnOEP at low (a) and high (b) magnifications.

These experiments demonstrate that the SnOEP-based photocatalytic seeding is crucial for the preparation of high-quality hollow platinum nanospheres. Additionally, it appears that platinum metal prefers nucleating and growing on the hydrophobic surface of polystyrene beads. This phenomenon agrees well with our previous observations using liposomes to template platinum growth, for which platinum metal preferably nucleates and grows within the hydrophobic liposomal bilayer[7,33]. An important factor that influences the quality of the generated hollow platinum spheres is the amount of SnOEP photocatalyst coverage on the beads. In our typical synthesis, the optimum surface area of the SnOEP molecules is calculated to be approximately 10 times that of the beads. This calculation compares the geometrical area of the spheres with an average diameter of 99 nm to the area of the SnOEP molecules, which are approximately 2 nm × 2 nm assuming the square planar molecule lies flat on the bead. Less SnOEP results in incomplete platinum coatings on the surface of the beads, while excess SnOEP leads to the formation of platinum not deposited on surface of the beads. The latter may occur because some SnOEP molecules are not adsorbed and function as isolated competing nucleation sites. Relying on the above understanding of the photocatalytic reaction, the thickness of the shells should be controllable by varying the amount of platinum complex available for growth and the light exposure. Indeed, the coverage of platinum on polystyrene beads can be controlled by simply reducing the concentration of aqueous salt from 8.8 to 4.4, 2.2, 0.55, and 0.28 mM at constant light exposure. As shown in Fig. 8, with the decrease of Pt(II) concentration the coverage on the polystyrene beads becomes increasingly incomplete as the size of the dendrites are reduced. At the lowest Pt concentrations, the fewer connections evident in the images would preclude shell

formation. In particular, for 4.4 mM Pt salt, more than 50% of the hollow platinum nanospheres fall apart after dissolution of the beads. In contrast, 8.8 mM Pt salt produces intact shells with few broken ones (Fig. 6c and d). This demonstrates that delicate control over shell thickness is practicable and that some control over the porosity of the Pt nanoshells is possible. At the lowest concentrations of 0.55 and 0.28 mM Pt salt, abundant Pt nanoparticles are observed on the beads. However, to attain intact Pt nanoshells thinner than 12 nm, many small dendrites would be required to allow them to join with neighboring ones to form the shell. These thin shells might be obtained by using a stronger light source to increase the seed density on the beads.

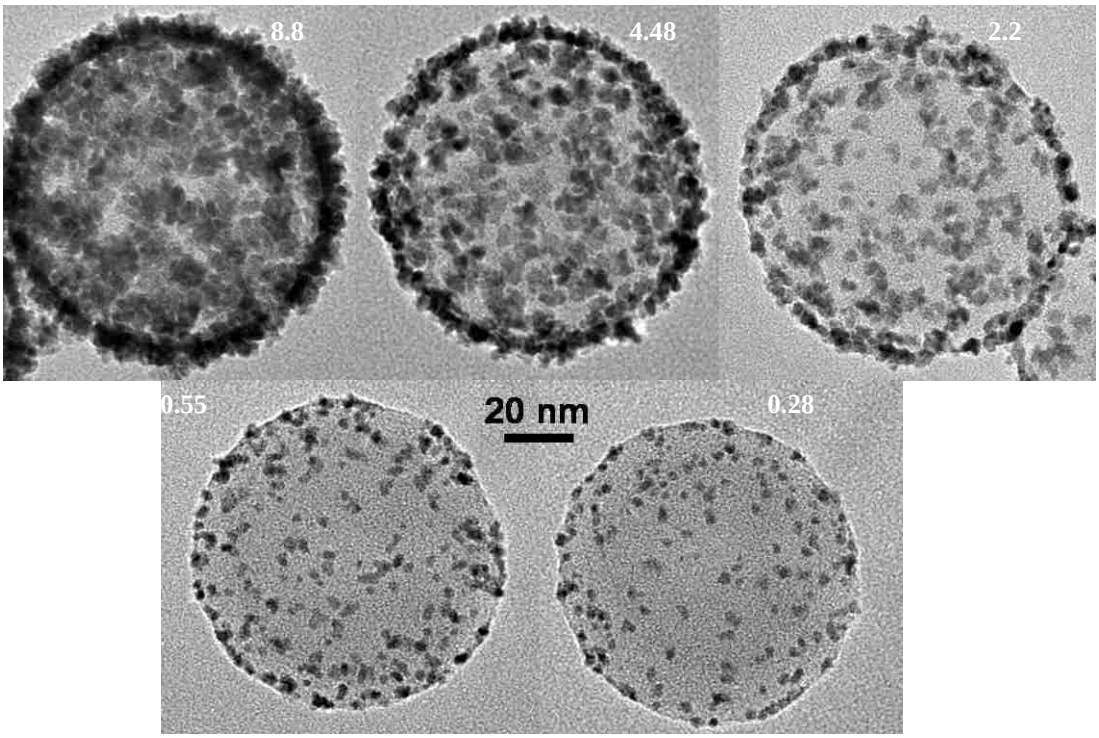

Figure 8: Bright-field TEM images of platinum nanostructures grown on polystyrene beads in the presence of 8.8, 4.4, 2.2, 0.55, and 0.28 mM platinum complex, respectively.

Chapter 4

Directed Growth of Platinum Nanostructures in an Inhomogeneous Reaction Environment

(To be submitted, Langmuir, 2010)

Nanostructured platinum is of particular interest because of its various environmental and energy-related applications that include sensing[34,35], reduction of tailpipe emissions[36,37], electrocatalytic energy conversion in proton exchange membrane (PEM) fuel cells[2,38,39], and renewable energy production in artificial photosynthesis and water-splitting devices[40,41]. However, the urgent request to limit the platinum usage owing to high cost and limited supply necessitates the optimization of activity and durability of platinum materials. In this regard, nanostructuring the morphology of platinum, including by templating strategies, has been widely adopted as an effective approach to improve platinum efficiency[5,8,42-44].

Among a wide range of templating agents, bicelles or disc-like micelles are a rare form of long chain/short chain lipid or lipid/ detergent assemblies[45]. Two oppositely charged single-chain surfactants or a block copolymer on its own can also self-assemble into bicelles[46-49]. Studies related to bicelles have mainly concentrated on their alignment and their biophysical and biochemical use as biomimetic membrane models, especially for reconstitution of membrane proteins[50-54]. From the point of view of soft templates, bicelles offer a unique inhomogeneous reaction environment possessing both low curvature and high curvature regions within a single bi-layer disk. Such a special reaction environment may enable the synthesis of a variety of nanostructures with complex morphologies potentially suitable for improved activity and durability as well as building

up nanodevices. Although the utilization of bicelles as soft templates for the synthesis of nanomaterials has been recommended, prior to our recent study,[55] no examples of their successful use for this purpose have been reported partly because of the difficulty of producing bicelles with a relatively high yield[47,49].

Our earlier work mainly focused on the synthesis and structural characterizations of platinum nanowheels[22]. Herein, we investigated in detail the preparation of large bicelles and verified their presence ranging from 80 to 150 nm in diameter by using negative stain TEM for direct observation. This result provides clear evidence to support our previous speculation that unusually large bicelles exist in our reaction system[22]. In explaining the metal growth mechanism, we had tentatively suggested an outward radial dendritic growth pattern initiated at the bicellar center[22]. To verify this, we monitored the structural evolution process of the platinum nanowheels by stopping reaction at different stages of growth. Using this approach we successfully elucidated the formation processes, including nucleation, autocatalytic dendritic nanosheet growth confined within the bicelles, and flaring of the sheet at the edge of the bicelles. Based on this understanding of the reaction, we achieved additional synthetic control by the varying temperature, carbon chain length of the ammonium bromide surfactant, reagent concentration, and the metal complexes in combination with being subjected to powerful sonication while preparing bicellar stock suspensions. An interesting sintering-resistant property of platinum nanowheels, originating from the formation of holey sheets when the nanowheels were irradiated under an electron beam or heated in an oven. The platinum nanowheels also have promissing catalytic properties as measured by hydrogen adsorption/desorption and oxygen reduction reaction kinetics using rotating disk

electrode voltammetry. In particular the platinum nanowheels are shown to have electrochemical surface areas (ECSA), mass and specific activities comparable to a commercially available platinum black but possess improved stability as result of the conversion from dendritic sheets to holey sheets through a ripening process[43].

Materials and Methods

Materials. Potassium tetrachloroplatinate(II) (Sigma-Aldrich, K_2PtCl_4, 99.99%), octadecyltrimethylammonium bromide (Sigma-Aldrich, C18TAB, 98%), cetyltrimethylammonium bromide (Sigma-Aldrich, C16TAB, 95%), tetradecyltrimethylammonium bromide (Fluka, C14TAB, 99%), Dodecyltrimethylammonium bromide (Fluka, C12TAB, 99%), decyltrimethylammonium bromide (Alfa Aesar, C10TAB, 98%), octyltrimethylammonium bromide (Alfa Aesar, C8TAB, 97%), sodium perfluorooctanoate (Alfa Aesar, FC7, 97%), and L-ascorbic acid (Sigma-Aldrich, AA, 99%) were used as received. All aqueous solutions were prepared using ultrapure water from a Barnstead Nanopure water system (Chesterland, OH).

Preparation of Surfactant Assemblies: Bicellar stock suspensions were prepared by dissolving 36 mg of C16TAB (1mM) in 100 mL of ultrapure water with mild or strong ultrasonication using a water-bath cleaner or a ultrasonic processor (GEX 750), followed by the addition of 44 mg of FC7 (1mM). The resultant mixture was colorless and slightly opalescent. To study the effect of alkyl chain length of ammonium bromides on the formation of bicelles and their further use as templates, surfactant suspensions were also prepared by substituting C16TAB with 1mM of C8TAB, C10TAB, C12TAB, C14TAB, and C18TAB, respectively.

Negative Staining of Bicelles: The stock bicelles were treated prior to transmission electron microscope (TEM) imaging according to a standard protocol[56]. Typically, (i) clamp a standard holey-carbon-coated copper grid into a set of forceps with sharp tips; (ii) add one drop of bacitracin solution (0.1 mg/ml in water, Sigma-Aldrich) and let it set for one minute, followed by wicking away the bacitracin drop by touching the edge of the grid with a tissue while holding the grid at a 90° angle to the plane of the grid; (iii) place one drop of the stock bicellar suspension on the grid and wait for one minute before wicking away the liquid using the same method as described above; (iv) add one drop of the negative stain, ammonium molybdate (1 wt% in water, Sigma-Aldrich). After one minute the stain drop was wicked away and the grid was allowed to dry under ambient conditions.

Dynamic Light Scattering of Bicellar Suspensions: The equivalent spherical hydrodynamic diameter and the size distribution of the C16TAB/FC7 mixture under different solution conditions were determined by DLS measurements using a Beckman Coulter N5 Submicron Particle Size Analyzer with a 25mW He-Ne laser (632.8-nm), a 1 min acquisition time, and 5 min equilibration time at 25°C. The scattering angle was 90º, and the intensity autocorrelation functions were fitted using PCS control software (Version 2.02). The equivalent spherical hydrodynamic diameter and the size distribution were calculated with the regularization algorithm provided by this software. All the samples were measured as prepared without further dilution. The intensity is between 5 × 104 counts and 1 × 106 counts. Before experimentation, the DLS setup was tested using standard polystyrene micro-bead suspensions. For a disc-shaped object, the relation

between the disk radius and the hydrodynamic radius of the corresponding sphere (R_h) is[57]:

$$R_h = \frac{3}{2} r \left[\sqrt{1+\left(\frac{t}{2r}\right)^2} + \frac{2r}{t} \ln\left(\frac{t}{2r} + \sqrt{1+\left(\frac{t}{2r}\right)^2} \right) - \frac{t}{2r} \right]^{-1} \quad \text{Equation 1}$$

Here t is the thickness of the bilayer. Following Jung[58], we used an estimated value of t=3 nm for the bilayer thickness. Using the above equation and Mathcad 8 software to solve for the disk radius (r), the 144 nm DLS diameter is converted to a 190 nm bicellar diameter.

Synthesis of Metallic Nanostructures: In a typical synthesis, 10 mL of 20 mM aged K_2PtCl_4 solution[59] was mixed with 10 mL of surfactant mixture containing C16TAB (1 mM) and FC7 (1 mM), followed by the addition of 264 mg of AA as reducing agent. The reaction mixture was then swirled to fully dissolve AA and left at 25 ºC for at least 1h to ensure that platinum salt reduction was complete. Finally, black precipitates with transparent and colorless supernatant were observed. A series of additional syntheses was also conducted by varying one parameter each time while holding all the others constant. A) Varying the concentration of aged K_2PtCl_4 solution using 10 mL of 3, 5, 8 or 10 mM vs our optimized synthesis of 10 mL of 20 mM aged K_2PtCl_4 solution; B) Varying the temperature at 0 or 100°C vs the typical synthesis at 25 ºC; C) Varying the carbon chain length of the ammonium bromide salt using 10 mL of surfactant mixture containing 1 mM FC7 and 1 mM C8TAB or C10TAB or C12TAB or C14TAB or C18TAB vs the typical synthesis using 1 mM FC7 and 1 mM C16TAB; D) Varying the bicelle

concentration using 10 mL of surfactant mixture containing C16TAB/FC7 (5 mM/5 mM) or C16TAB/FC7 (10 mM/10 mM) vs C16TAB/FC7 (1 mM/1 mM).

Electron Microscopy: TEM (200 keV JEOL 2010), scanning electron microscopy (SEM, 1~30 keV Hitachi S-5200), and high-angle annular dark-field (HAADF) scanning TEM (STEM, 200 keV JEOL 2010F) were performed on the nanostructures. The platinum samples for TEM analysis were prepared by adding drops of colloidal solutions onto standard holey carbon-coated copper grids. The excess solvent was wicked away with a tissue paper, and the grids were dried in air. The platinum samples for SEM characterization were prepared using the same procedure with doped silicon wafers instead of holey-carbon copper grids. The samples were then washed at least three times with ultrapure water to remove salts and surfactant molecules and air dried for at least two hours before imaging.

Structural Evolution Study: TEM samples were prepared at specific times (30, 70, 90, 100, 110, and 120 minutes, and 48 hours) during the continuous reaction of a typical synthetic system by adding several drops of reaction mixture to a standard holey-carbon TEM grid, followed by washing with water and drying in the air to effectively interrupt the reduction of platinum complexes. This procedure gives a snapshot of the nanostructures present at that specific point in time.

Sintering Studies of Platinum Nanowheels: In furnace (Thermolyne 48000) sintering experiments, the platinum nanowheels were placed onto a doped silicon wafer and heated for one hour at each temperature of 100, 200, 300, and 400 °C under atmospheric conditions. For the electron beam sintering of the nanowheels, the sample was loaded onto a holey-carbon coated copper grid using the same procedure as described above. A

representative platinum nanowheel was selected for extended electron beam irradiation by a high current density electron beam (approximately 90 pA/cm^2) provided by a TEM (JEOL 2010) operating at 200 KeV and 15 K magnification. Images were taken every 2.5 minutes.

Electrochemical Measurements: Electrochemical measurements were performed using a glassy carbon (GC) disk (Pine Instruments, 5 mm diameter, 0.196 cm^2) rotating ring disk electrode (RRDE, Pine Instruments) in which the platinum ring was not utilized (ie. a rotating disk electrode (RDE) configuration). The RRDE was connected to a Pine Instruments AFCBP1 bipotentiostat with analytical rotator for all potential cycling and sweep voltammetry. A Pine Instruments Ag/AgCl electrode (3.3M KCl) was used as the reference electrode. The counter electrode was a platinum wire. A standard 3 port electrochemical cell served as the reaction vessel. The electrolyte used was 0.5 M sulfuric acid (Mallinckrodt Standard) diluted with nanopure water (Barnstead Nanopure Water System, 17.8 MΩ/cm^3) from a 1M stock solution. All potentials obtained in reference to the Ag/AgCl electrode have been converted to the reversible hydrogen electrode for this report.

Working Electrode Preparation: Before loading platinum, the GC disk was polished with 0.05 micron alumina paste (Buehler) to a shiny mirror-like surface. Catalyst slurries were prepared by dispersing 8 mg of platinum catalyst in a mixture of 0.4 mL of isopropanol (Aldrich, 99.5%, ACS Reagent), 3.6 mL deionized water and 20 μL of 5 wt% Nafion perfluoronated ion exchange resin (Aldrich) by ultrasonication. To prepare the electrode a 20 μL aliquot of the suspended materials was pipetted onto the glassy carbon disk and allowed to dry under ambient conditions resulting in a platinum loading

of approximately 0.2 mg/cm^2. The platinum loaded GC disk was then inserted into the RRDE tip and used as the working electrode.

Brunauer Emmett Teller (BET) Surface Areas: The BET surface area of the platinum nanowheels was determined by N_2 adsorption experiments. The samples were degassed at 50°C and 0.01 Torr for at least 12 hours before measurement. The surface area measurements were conducted using an Autosorb-6 Quantachrome Instrument (Boynton Beach, FL). The surface area was then calculated from the BET equation using a nitrogen molecular area of 0.162 nm^2. The linear region between 0.05 and 0.3 relative pressures gives a least squares coefficient $R^2 > 0.999$ for at least 7 adsorption points.

Determination of Electrochemical Surface Areas (ECSA): After deaeration of the electrolyte solution with argon gas (Matheson Tri-Gas, Technical Grade) for at least 30 minutes the working electrode was immersed into the electrolyte at a rotation rate of 1600 RPMs and the potential was cycled from 0.05 to 1.2 V (RHE) at a sweep rate of 0.05 V/s at least 3 times to obtain a stable hydrogen adsorption/desorption cyclic voltammogram. The average Coulombic charge density Q_H (C/m^2) based on the geometric surface area of the electrode is determined from the hydrogen adsorption/desorption region of the voltammogram from 0.05 to 0.4 V (RHE) (further explanation of this calculation is available in Appendix A). The ECSA (m^2_{Pt}/g_{Pt}) was then calculated from equation 2:

$$ECSA = \frac{Q_H / Q_m}{W} \qquad \text{Equation 2}$$

Where Q_m (2.1 C/m^2_{Pt}) is the assumed charge density for monolayer adsorption of hydrogen onto an active polycrystalline platinum surface[60] and W is the platinum loading

on the electrode (g/m^2). The value for Q_m is reasonable given that the platinum nanowheels were previously shown to be polycrystalline using X-ray diffraction[22].

Determination of Mass and Specific Activity: The mass and specific activities were determined from analysis of the oxygen reduction reaction (ORR). Background voltammograms for the capacitive currents were generated by first deaerating the electrolyte solution with argon gas for at least 30 minutes then performing linear sweep voltammetry from 0.05 to 1.2 V (RHE) at a sweep rate of 0.005 V/s at 1600 RPMs and saving the obtained data for later subtraction from the oxygen reduction reaction data. For the ORR the electrolyte was saturated with oxygen gas (Matheson Tri-Gas, Technical Grade) for at least 30 minutes and the linear potential sweep was repeated using the same parameters. The background capacitive currents were then subtracted from the oxygen reduction reaction data and divided by the geometric surface area of the GC disk to generate a polarization curve. The mass activity was then calculated from equation 3[61]:

$$A_m = \frac{i_{PolDensity}}{W} \quad \text{Equation 3}$$

Where A_m is the mass activity (mA/mg), $i_{PolDensity}$ is the polarization current density (mA/cm^2) normalized for the geometric surface area of the electrode at 0.9V and W is the platinum loading on the working electrode (mg/cm^2).

The specific activity was calculated according equation 4[61]:

$$A_s = \frac{i_{Pol}}{S_r} \quad \text{Equation 4}$$

Where A_s is the specific activity (mA/cm^2_{Pt}), i_{Pol} is the polarization current (mA) at 0.9V, and S_r is the effective ECSA (cm^2_{Pt}) for the mass of catalyst used. Further details of these calculations can be found in Appendix A.

Results and Discussion

Preparation and Characterizations of Bicellar Suspension: Bicelles are a rare class of soft assemblies with disk-like shape. Using an equimolar mixture of C16TAB and FC7 bicelles can be prepared as shown in figure 9. Prior to our recent study using an aqueous C16TAB/FC7 mixture with equimolarity and a total 0.08 wt% surfactant to prepare high-yield and large bicelles[22], only low-yield and small bicelles (35 ± 4 nm in mean radius) were obtained from a C16TAB/FC7 mixture with 2 wt% total surfactant and a molar ratio of 20:80 by Jung and coworkers[58]. In our work, we also demonstrated the synthesis of abundant platinum nanowheels with a large average diameter in the presence of templating CT16AB/FC7 bicelles. The obtained large platinum nanowheels suggest that the size of bicelles in our reaction system may be as large as that of the nanowheels. Additionally, the abundance of the nanowheels indicates that bicelles may be the dominant species in the reaction system. As a consequence, we previously proposed the existence of high-yield and large bicelles in our system. However, direct evidence was not provided in our earlier study. Herein, bicelles were directly revealed by negative stain TEM. Figure 10a shows that bicelles appear as white lines with a typical length about 100 nm. Since Jung et al. reported that the CTAB/FC7 bicelles or bilayer discs appear as narrow lines[58], it is certain that the white lines in Figure 10a are also bicelles. This clearly proves that large bicelles do exist in our reaction system, confirming our previous speculation. Figure 10a shows that bicelles are the major products coexisting with other minor mesostructures without well defined morphologies. Recently, when investigating the C16TAB/FC7 mixed surfactant system at the 1:1 molar ratio using deuterium nuclear magnetic resonance (^{2}H NMR) spectroscopy, Alam and McIntyre found that a lamellar

phase (possibly bicelles) is the dominant species at room temperature and a relatively low total wt% surfactant, which agrees well with our observation[62]. DLS measurements of the stock bicelles gave an average hydrodynamic size of 144 nm as shown in Figure 10b. DLS analysis assumes samples are spherical in shape which bicelles are not, therefore we converted the hydrodynamic size of equivalent spheres (144 nm) to the diameter of bicelles (190 nm) from equation 1 in the materials and methods section[57]. The calculated bicellar diameter (190 nm) is larger than the TEM results (100 nm) possibly due to the presence of minor mesophases other than bicelles. Additionally, DLS reveals a characteristic increase in the size of the bicelles to 602 nm in the presence of the platinum complex and ascorbic acid which is most likely due to changes in ionic strength, pH and bicellar aggregation. This increase in bicelle size is in relatively close agreement with the size of the observed platinum nanowheel products. Nevertheless, the existence of relatively large bicelles in our system is certain and can provide an interesting soft template suitable for directing the growth of platinum nanostructures.

a

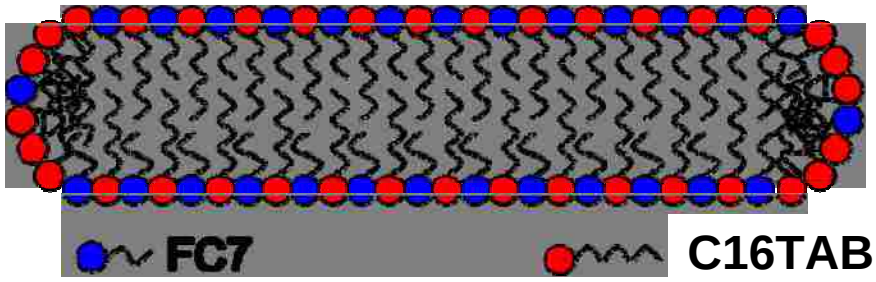

b

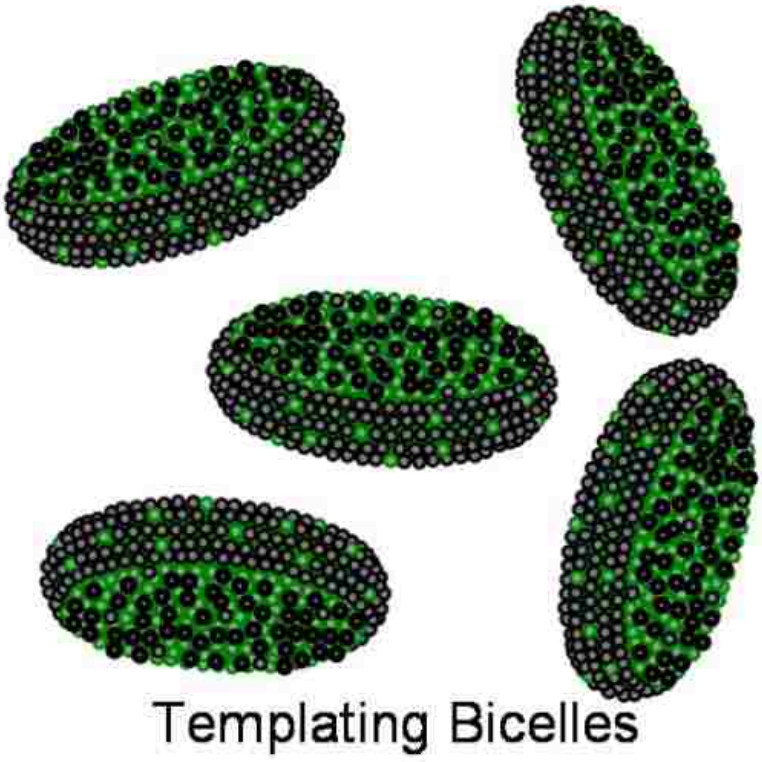

Figure 9: a) Cross-sectional view of a bicelle composed of C16TAB and FC7, b) disk-like bicelle assemblies which can be used as a template for metal growth.

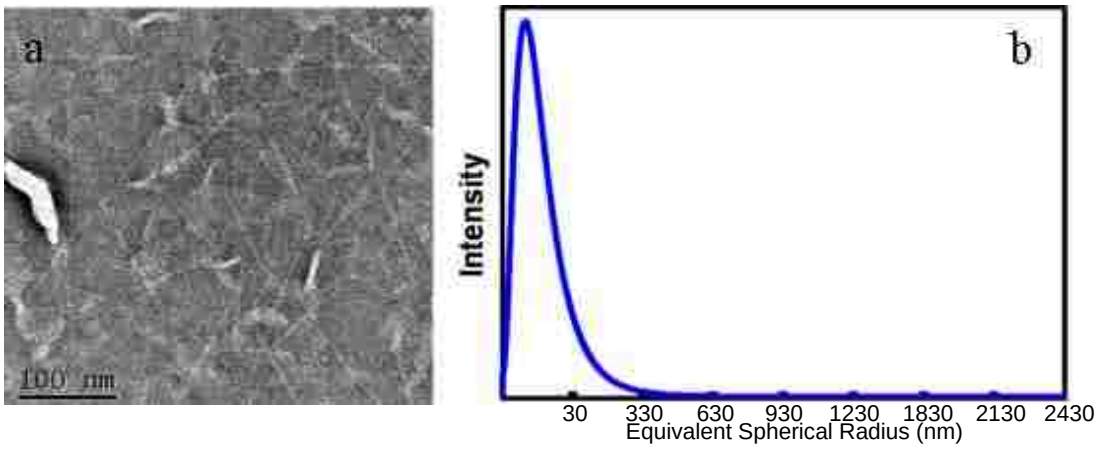

Figure 10: (a) TEM image of stained C16TAB/FC7 Bicelles (1mM in C16TAB and FC7); (b) DLS radius size distribution measurement of stock C16TAB/FC7 bicelles (1mM in C16TAB and FC7).

Formation Mechanism of Bicelles-Templated Platinum Nanostructures: Black precipitates with colorless and transparent supernatant were observed after allowing a typical reaction system to react under ambient conditions. SEM analysis (Figure 11a) revealed that abundant circular platinum nanostructures with an average diameter of 496 ± 55 nm were produced. The circular nanostructures are actually platinum nanowheels with thickened center, flat sheet-like dendritic interior and flared edges (Figure 11b and Inset), which have been fully characterized previously[22]. The radial dendritic sheet region is approximately 3 nm in thickness as measured from HAADF-STEM enhanced contrast imaging. The presence of bicelles in the reaction system plays an important role in confining the growth of platinum nanowheels, since only platinum chunks without well-defined morphology were obtained in the absence of templating bicelles. However, the detailed formation process of the nanowheels remained unclear.

To gain more understanding about the growth process of the wheels produced by the bicellar templating method, drops of reaction mixture were taken out at specific reaction times from a running reaction system to prepare TEM samples. Rinsing the TEM grids with Nanopure water effectively interrupts the reaction and allows us to obtain a snapshot of the structure present at that specific reaction stage. Representative TEM images are shown in Figure 12. At 30 minutes of reaction (Figure 12a), few individual particles are found on the TEM grid. At this early stage of the reaction, it is not a surprise to observe very few platinum nanostructures. By 70 minutes, the reaction mixture has turned black. This indicates that a significant amount of colloidal structures have already formed. TEM analysis confirmed that many 10-40 nm particles have been produced (Figure 12b). These nanoparticles are likely initial nucleation centers of

platinum nanowheels. By 90 minutes, more and larger nanoparticles are seen (Figure 12c), and at 100 minutes (Figure 12d), the original nanoparticles (seeds) have begun to grow into dendritic nanosheets and most of them already have many branches. This verifies that the nanoparticles observed during the first 90 minutes of reaction are almost entirely nucleation sites, which become the thickened centers of final nanowheels. After 110 and 120 minutes of reaction (Figure 12e, f), the two-dimensional dendrites with a thickened center have grown larger and larger in a roughly circular pattern. At 120 minutes and beyond (Figure 12g), we propose that the growth of dendritic nanosheets has reached the edge region of bicelles, where the reaction environment transitions from a flat bilayer to a highly curved and crowded edge, and such a reaction environment variation may eventually lead to flaring out of the growth of dendritic sheets, forming thickened edges of nanowheels. Alternatively, it is possible that the growth of dendritic sheet penetrating bicelles contributes to the structural flaring. It is worth noting that at the late reaction stage some growth perpendicular to the plane of nanowheels occurred randomly, but this is not the dominating growth pattern and does not modify the overall wheel-like structure much (Figure 12g). The study on structural evolution with time discloses that the confined growth of nanowheels in bicelles consists of nucleation, outward radial dendritic growth, and flaring out.

Additionally, it is necessary to point out that almost all the initial nucleation centers reside in the center of wheels. Although there have yet to be solid explanations for this phenomenon, we speculate that an electric field originating from enriched positive charges distributed on the bicellar outer edge might influence the positioning of initial nucleation centers provided that nanoparticles always carry certain types of net charges

on their surface. Another contributor might be that the bicelles central regions are mechanically more compliant when compared with the bicellar edges, where the bilayer is more rigid. This loosening may allow bicelles to more easily accommodate original growth of nucleation centers. Based on the high-yield of bicelle templated product as observed in figure 11, a large percentage of the initial nucleation centers are believed to form fully developed platinum nanowheels after the reduction process is complete.

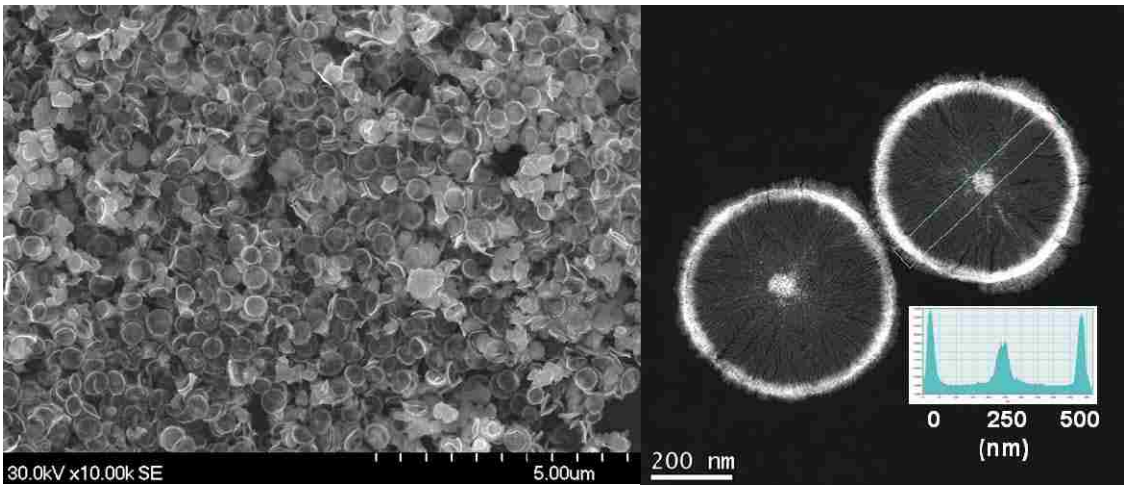

Figure 11. SEM (a) and HAADF scanning-TEM image (b) of platinum nanowheels (Inset: platinum density profile crossing the selected rectangular region of a wheel in (b)).

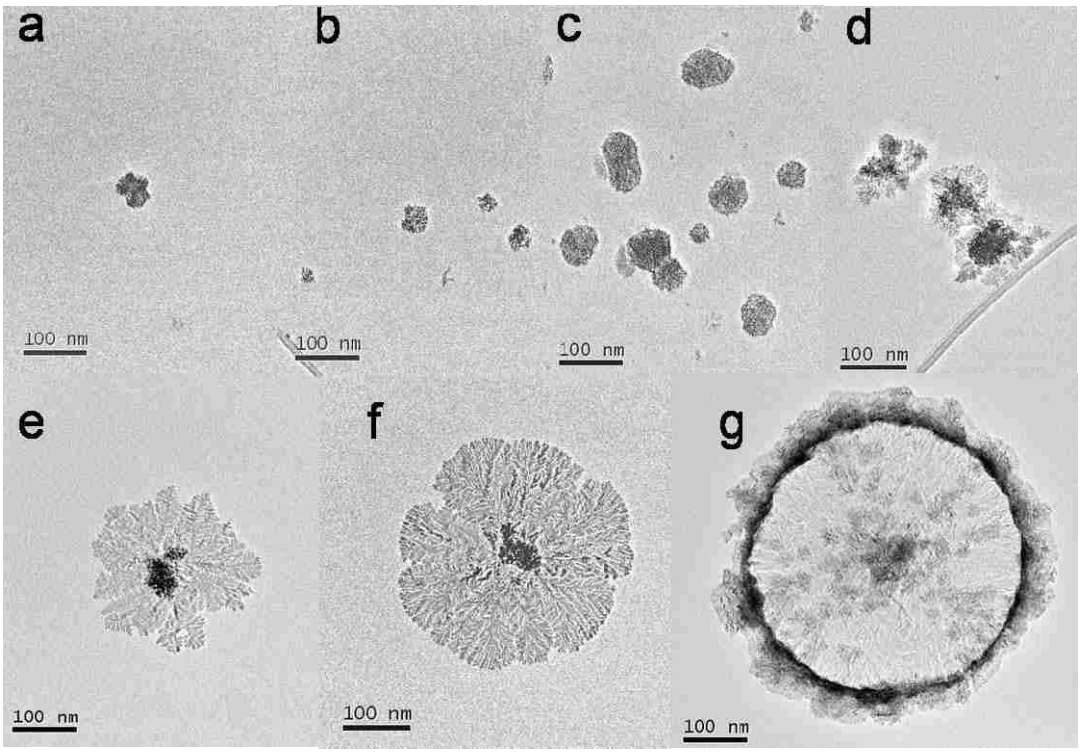

Figure 12. TEM images of platinum nanostructures obtained at different reaction times: (a) 30, (b) 70, (c) 90, (d) 100, (e) 110, and (f) 120 minute, and (g) 48 hours.

Controlled Synthesis: Based on a developing understanding of the formation mechanism of the nanowheels, a series of controlled synthesis were conducted by simply varying reagent concentration, carbon chain length of CTAB, metal resource, and concentration of C16TAB and FC7.

Concentration of platinum complex: By lowering the concentration of platinum complexes and holding all other reaction parameters constant, the reaction can be terminated at any stage identified in the above structural evolution study, thereby allowing us to achieve various final products as shown in Figure 13. At a low concentration of platinum complex (1.5 mM), the reaction ended at the nucleation stage and only seed particles with a typical diameter of 50-70 nm were obtained (Figure 13a). With the increase of concentration of platinum complexes, dendritic sheets start growing out of the seeds. It turns out that the size of dendritic sheet part is tunable by varying the concentration of platinum complex (Figure 13b-e). Additionally, it appears that when the concentration of platinum complex is below 5 mM, the obtained platinum nanostructures are not circular, indicating an anisotropic growth pattern. In contrast, for the case of 5 and 10 mM of platinum complex used in the synthesis the final products are nearly circular possibly because additional growth of dendritic sheets fills up the empty space in parallel with a confining effect arising from bicelles.

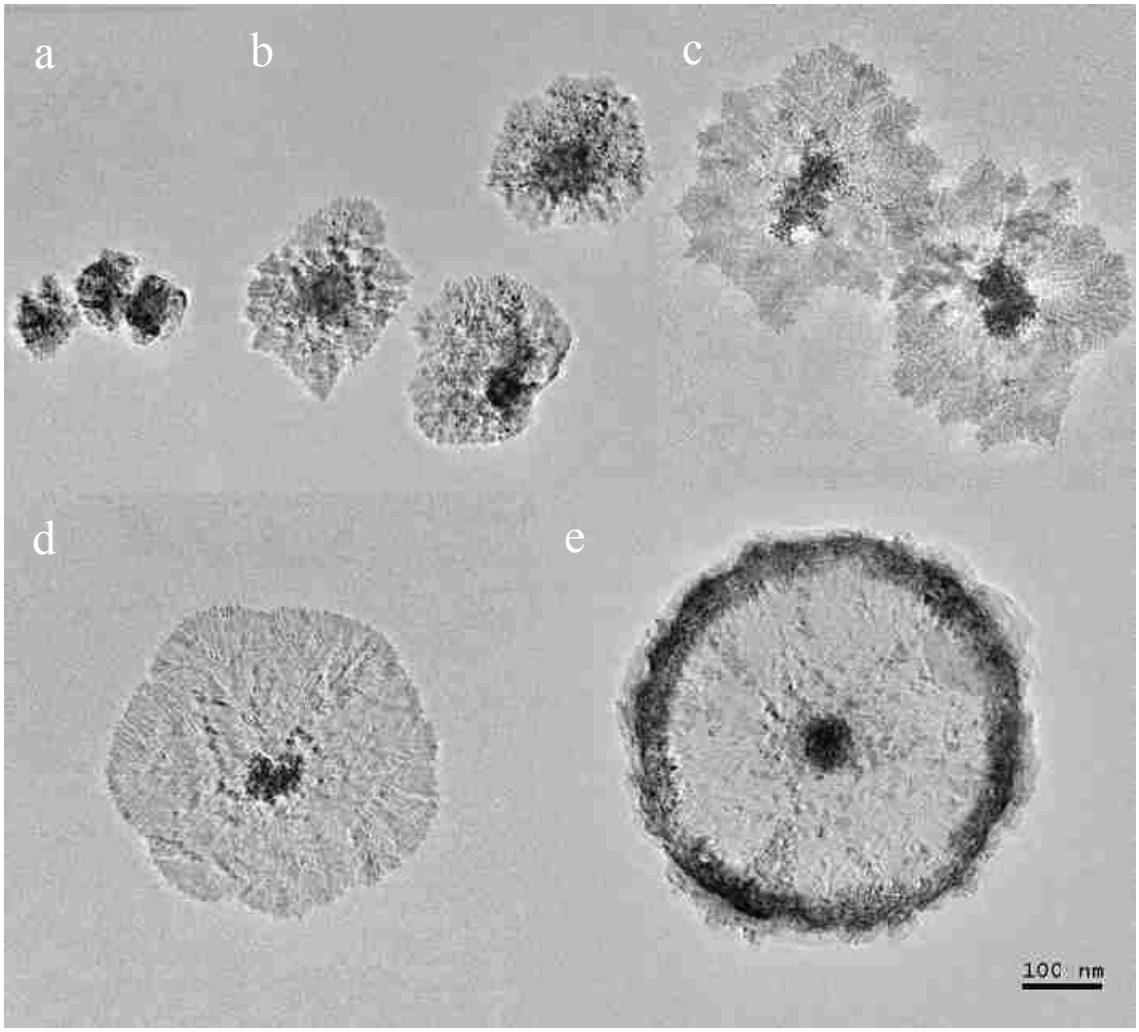

Figure 13. TEM images of platinum nanostructures obtained at different concentration of platinum complex: (a) 1.5, (b) 2.5, (c) 4, (d) 5, and (e) 10 mM.

Carbon chain length of CTAB: 1 mM of C8TAB, C10TAB, C12TAB, C14TAB, and C18TAB were used to replace C16TAB for the synthesis of platinum nanowheels, respectively. Evidently the length of carbon chain does not have a significant effect on the synthesis of platinum nanowheels except in lowering the overall yield of nanowheels in an undesirable manner. This is likely due to unideal interactions between the ammonium bromide surfactants altered tail lengths and the unaltered FC7. From this it was determined that C16TAB provides the optimum chain length for a high yield of platinum nanowheels when used with FC7. It may be possible to obtain a higher yield of bicelles of different sizes by increasing or decreasing the chain lengths of the CTAB and FC7 analogs in a proportional manner.

Sintering studies: Durability of nanostructured platinum is of particular interest since it is directly correlated to usage efficiency and represents a primary quality of the materials. From a practical application point of view, more durable platinum nanostructures are always desired. Recently, our group found that under irradiation of an electron beam in TEM dendritic platinum nanosheets structurally evolve into meta-stable holey-nanosheets thus providing an interesting resistance to sintering superior to semi-spherical platinum nanoparticles[43]. This shape-related sintering resistance was further explored by Monte Carlo simulations and experimentally corroborated by fuel cell tests[43]. As platinum nanowheels contain a large portion of dendritic sheets, we expect that similar metastable nanoholes would form in wheels under an electron beam irradiation.

To confirm this, a specific nanowheel was selected and irradiated with a TEM electron beam. Figure 14 shows that the original dendritic sheet part of the wheel gradually evolved into a holey-nanosheet as expected. Before the electron beam irradiation, the

dendritic features are prominent and well-defined (Figure 14a). After 5 minutes of irradiation, the dendritic arms and nano-crevices among them are obscured and some nanoholes have already started to form. At 10 minutes, there are more nanoholes formed accompanied with the disappearance of the dendritic features of the nanosheet. When the wheel was irradiated for 20 minutes, its dendritic sheet region has already evolved into a holey-sheet with 2-5 nm holes embedded. The size of the holes is similar to those observed before in our dendritic nanosheets[43]. This suggests that the nanowheels should also possess the property of being resistant to a sintering process dominated by atomic surface diffusion. At 30 and 35 minutes, most of the nanoholes remain. This study shows the dendritic sheet region of a nanowheel evolves into a desired holey-sheet, likely making the nanowheel resistant to atomic diffusion mediated sintering analogous to dendritic platinum nanosheets[43].

Sometimes nanostructured platinum needs to be employed in an environment with elevated temperatures. Thus, thermal stability of platinum nanowheels is another crucial property that needs to be considered with respect to real applications. Therefore, we have examined structural response of nanowheels to high temperatures. The platinum nanowheels were first loaded onto doped silicon wafers by drop casting and then placed into a furnace under atmospheric conditions at different temperatures. After one hour of heating in an oven operated at 100 ˚C as shown in Figure 15a, platinum nanowheels remain structurally stable and no structural modification can be observed. After one hour of heating at 200 ˚C, platinum nanowheels are still stable and most of their dendritic features remain. It is noticeable that nanowheels have already structurally evolved and a few nanoholes are discernable. One hour of heating at 300 ˚C led to loss of dendritic

features and formation of larger nanoholes and a few isolated platinum islands. The platinum nanowheels obviously sinter around 300 ˚C, indicating that nanowheels cannot survive temperatures above to 300 ˚C. After experiencing one hour of heating at 400 ˚C, nanowheels sinter even more and discrete platinum islands ranging from 20 to 60 nm formed, completely replacing the original dendritic sheet-like interior (Figure 15d).

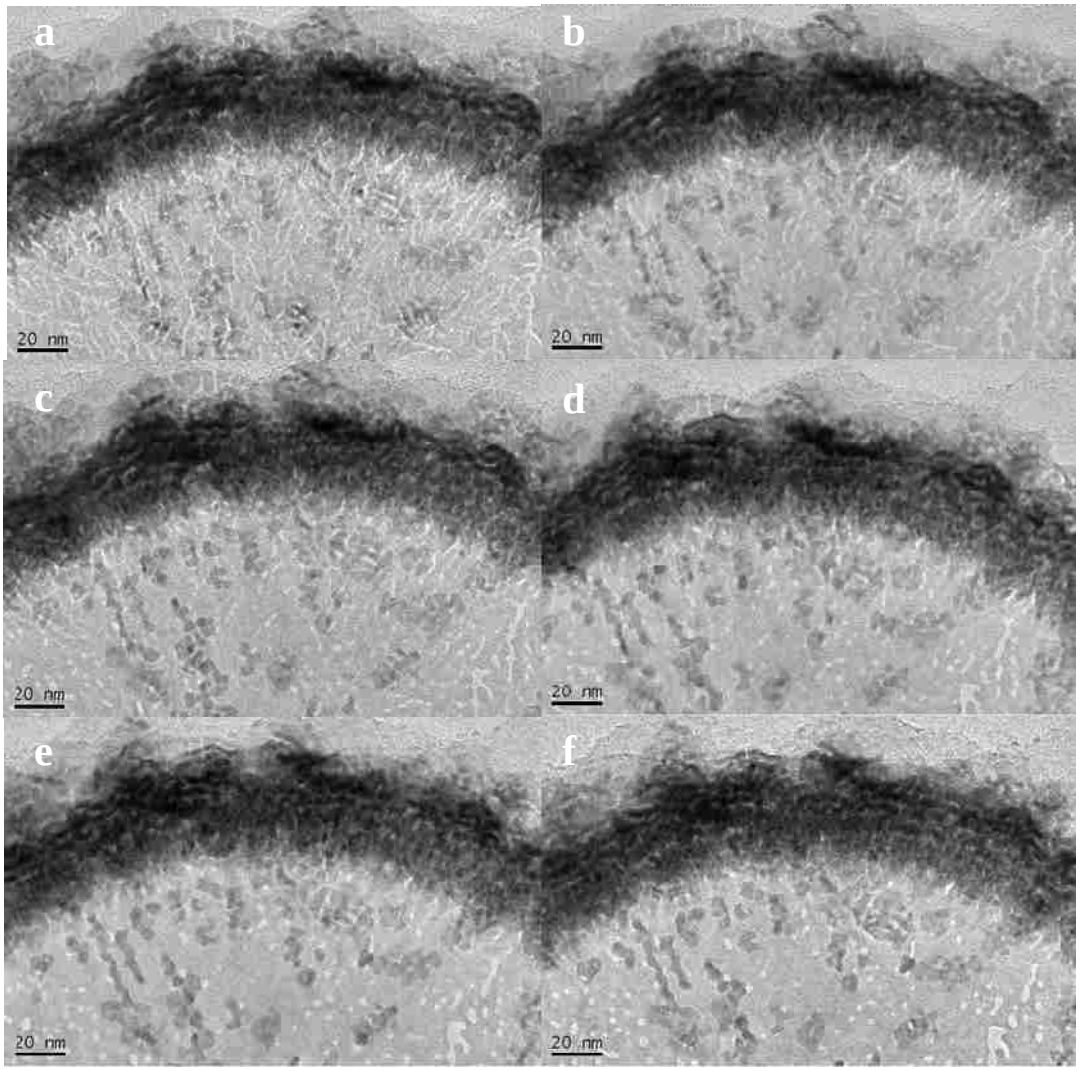

Figure 14. TEM images of a portion of a platinum nanowheel under TEM electron beam irradiation (200 kV, 90pA/cm^2) at different times: (a) 0, (b) 5, (c) 10, (d) 20, (e) 30, and (f) 35 min.

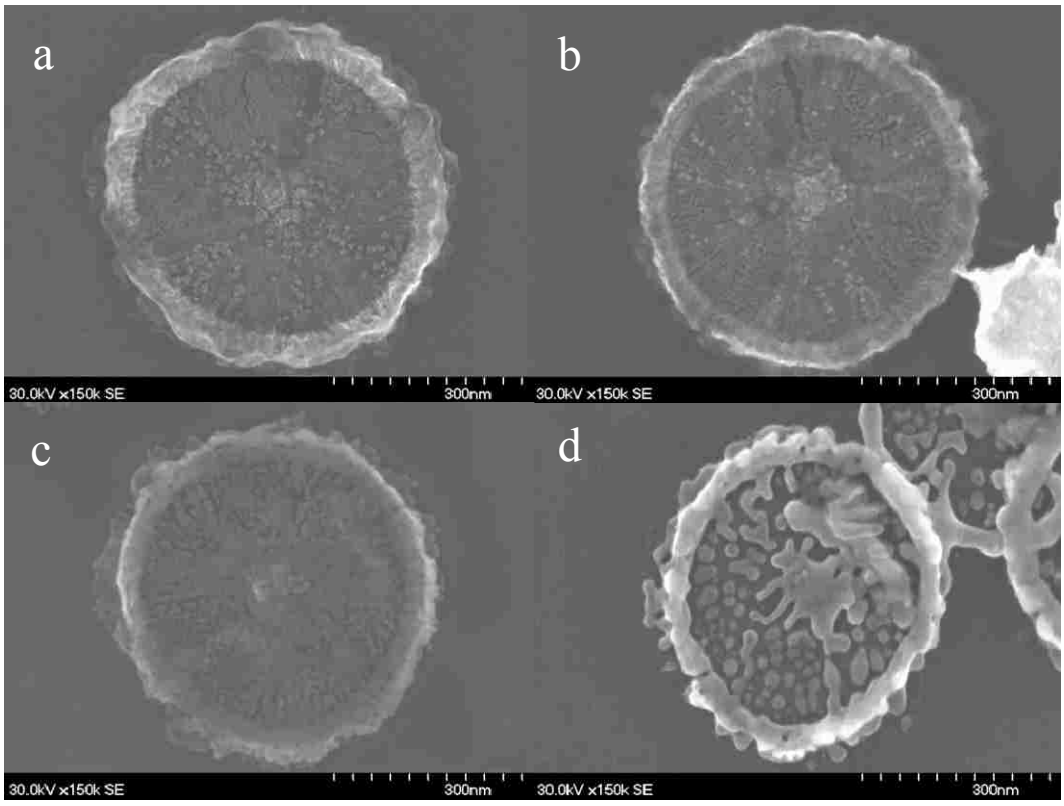

Figure 15. SEM images of platinum nanowheels after being heated in an oven for one hour at different temperatures: (a) 100, (b) 200, (c) 300, and (d) 400˚C.

BET Surface Area: The BET surface area of the platinum nanowheels was determined to be 35 m^2/g. E-TEK platinum black has literature values[33,63] of 30-34 m^2/g for the BET surface area. The difference in the BET surface areas is essentially negligible.

Electrochemical Analysis: The ECSA, mass and specific activities are important measures of catalyst performance and quality. The cyclic voltammograms for hydrogen adsorption/desorption in the platinum nanowheels and commercial platinum black (E-TEK) are shown in figure 16 and were used to determine the average charge densities and ECSA values. The average charge densities (Q_H) calculated in the region from 0.05 to 0.4 V (RHE) were determined to be 7.26 and 8.56 mC/cm^2 for the platinum nanowheels and platinum black respectively. The ECSA of the platinum nanowheels was then determined from equation 2 in the materials and methods section to be 17.05 ± 0.30 m^2_{Pt}/g_{Pt}, which is reasonably close to the value obtained for the E-TEK platinum black of 20.10 ± 1.20 m^2_{Pt}/g_{Pt}. This slight difference in ECSA is of little concern when one considers the stability improvement gained in the formation of holey-sheets in the case of the platinum nanowheels.

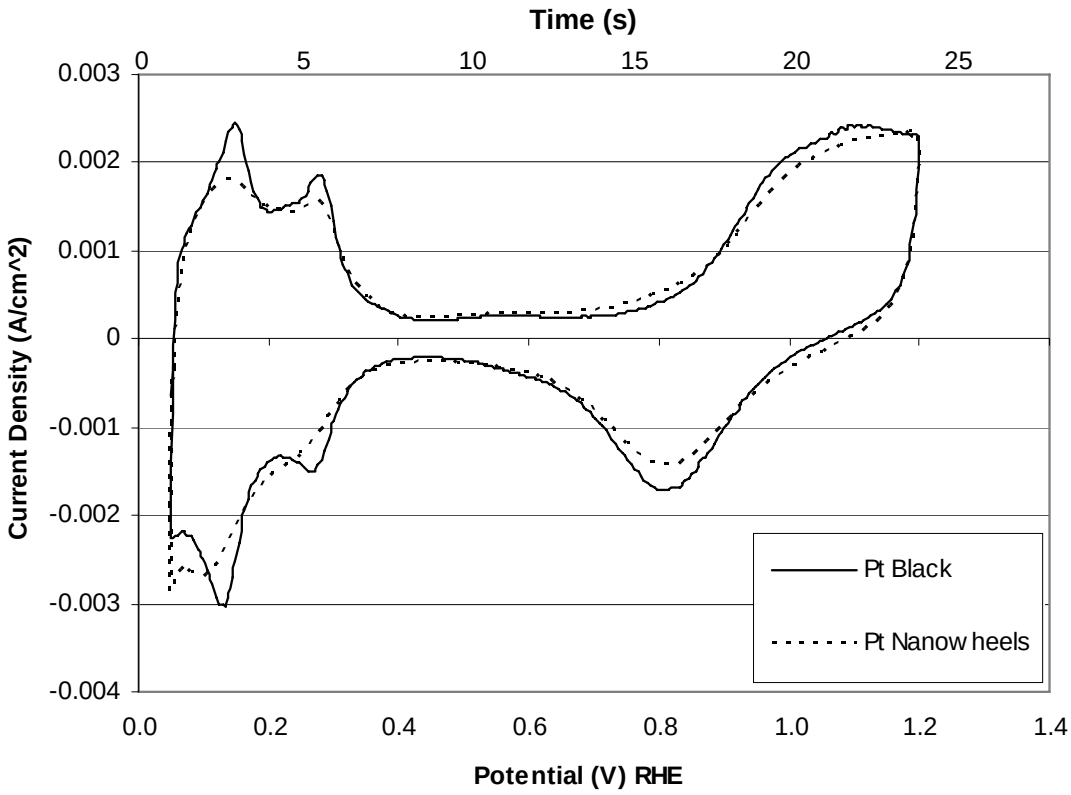

Figure 16: Hydrogen adsorption/desorption cyclic voltammograms for the platinum nanowheels and commercially available E-TEK platinum black.

From this observation it can be reasonably expected that although the nanowheels posses a slightly smaller ECSA, the performance of the platinum black would degrade at a much faster rate than the platinum nanowheels under strenuous conditions because of it's susceptibility to atomic diffusion mediated sintering at the interfaces of the small particles.

The mass and specific activities are two important parameters that determine catalyst quality and efficiency by gauging its ability to exchange current based on mass and the effective electrochemically active surface area. The polarization curves for both platinum black and the platinum nanowheels are shown in figure 17. The mass activities (A_m) were determined from the polarization curve current density at 0.9V and found to be 3.48 and 3.98 mA/mg_{Pt} for the platinum nanowheels and platinum black, respectively. Again, the performance of the platinum nanowheels is very close to that of the platinum black thus reinforcing its potential use as electrocatalyst based on improved durability. The specific activities (A_S) also determined from the polarization curve were determined to be 20.0 and 19.7 $\mu A/cm^2$ for the platinum nanowheels and platinum black respectively. The difference in specific activity is essentially negligible and further serves to support the platinum nanowheels as a potential candidate to replace the platinum black electrocatalyst based on its improved stability.

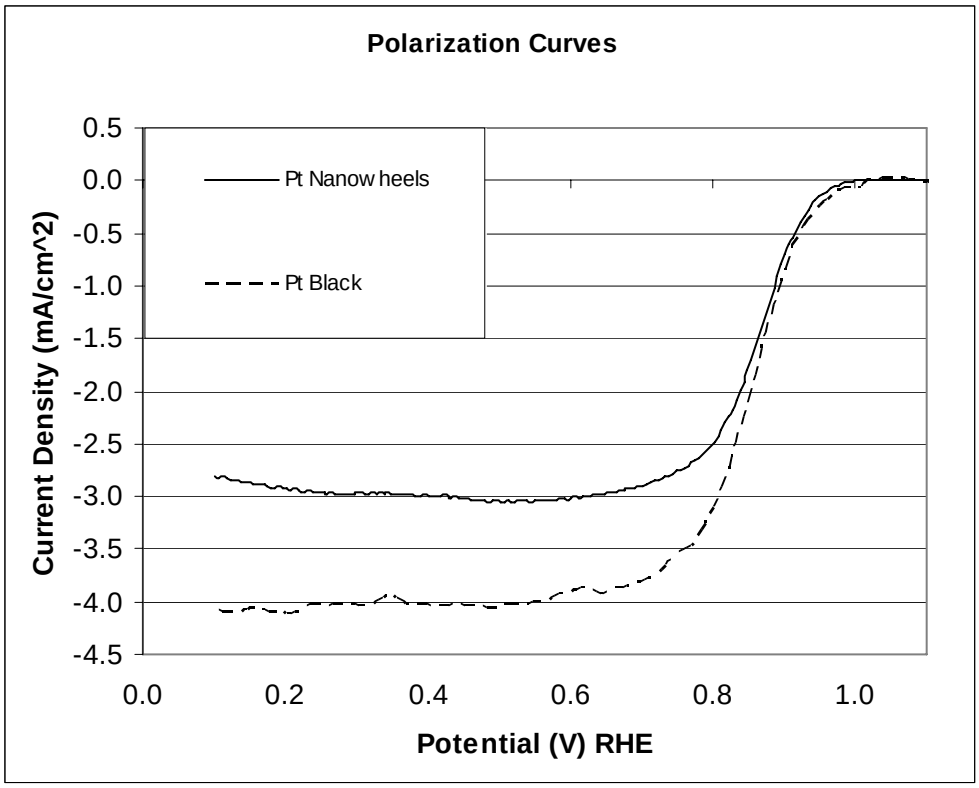

Figure 17: Polarization curves for Pt Black and Pt Nanowheels

Conclusion

We have shown that a high yield of large bicelles exists in an equimolar system that contains CTAB and FC7. The bicelles provide a unique inhomogeneous reaction environment possessing both low curvature and high curvature regions with a hydrophobic interior. These bicelles have been used to template the growth of platinum dendritic nanowheels with thickened centers, and flared edges. From the time-based evolution study of the platinum nanowheels the growth mechanism was determined to follow a radial dendritic growth pattern from a centrally-located nucleation seed which continued until growth reached the highly curved edge region upon which edge flaring occurs. Variation of the concentration of platinum complex yielded comparable results showing that at low concentrations only platinum seed particles are obtained, and with increasing concentration the radius of obtained products increases until it reaches the curved bicelle edge region. Once the bicelle edge region is reached edge flaring occurs until the platinum complex is used up. A study on the effect of the carbon chain length of the ammonium bromide surfactant revealed that the use of C16TAB provides an optimum yield of bicelles which can be used as a template for metal growth. Sintering studies using both thermal heating and irradiation of the nanowheels by TEM revealed an unusual stabilizing property based on the ripening of the platinum nanowheels into meta-stable holey-sheets, similar to our previously produced platinum dendritic sheets[43]. In addition, the platinum nanowheels have comparable ECSA, mass and specific activities with commercially available E-TEK platinum black but because of the aforementioned improvement in stability may be a better choice of electrocatalyst in many applications.

Chapter 5

Discussion and Conclusion

Summary

Using a bottom-up approach the successful synthesis of two types of platinum nanostructures has been demonstrated. A hard templating method which utilized latex beads with adsorbed porphyrin catalyst in conjunction with a photocatalytic seeding strategy was used in developing porous platinum hollow spheres. The growth mechanism is shown to consist of rapid nucleation of large amounts of platinum seeds on the bead surface followed by an increase in size until they become autocatalytic leading to the formation of linked small globular dendrites which coat the beads. Etching of the templating latex beads using chloroform results in the final product of porous platinum hollow spheres.

A soft-templating strategy utilized aqueous bicelles as a template for growth of dendritic platinum nanowheels with thickened centers and flared edges. The platinum nanowheels exhibit a radial dendritic growth pattern as indicated by a time-evolution study and platinum complex concentration study. The thickened centers are likely the initial nucleating seed particles. Edge flaring occurs when radial dendritic growth enters the highly curved edge region of the templating bicelles. Sintering studies using thermal heating and TEM irradiation reveal an unusual stability in the platinum nanowheel based on a ripening transformation to meta-stable nanoporous holey-sheets. This unusual characteristic prompted further study of the platinum nanowheels for use in electrocatalytic applications. Electrochemical measurements of the ECSA, mass and specific activity revealed that the platinum nanowheels have comparable initial

performance with commercially available E-TEK platinum black catalyst. The platinum nanowheels do provide a distinct advantage over platinum black in that they exhibit increased durability as result of the formation of holey-sheets. This increases the useable lifetime of the platinum nanowheels and supports their potential use as a replacement for platinum black in demanding high energy application such as in the proton exchange membrane fuel cell. As a result of nanoscale engineering, both the platinum hollow nanospheres and platinum nanowheels offer increased surface to volume ratios. This important trait can reduce the amount of required precious metal in catalytic applications.

Implications for future research

Both the platinum hollow nanospheres and nanowheels have potential applications in the fuel cell industry as well as numerous other catalytic applications which require the precious metal. The nanoscale features give them a distinct advantage over their bulk material counterparts aiding in cost reduction, efficient material usage and improved catalytic efficiency. Given the remarkable durability obtained when the platinum nanowheels evolve in to meta-stable holey-sheets they would benefit from further study in an actual device. Fabrication of membrane electrode assemblies (MEA) could provide real fuel cell performance and kinetic data for the nanostructures (performance within a fuel cell sometimes differs from the idealized tests run on the lab scale). Successful commercialization of these platinum nanostructures would require testing on a larger scale, including testing in actual devices. In addition, should be considered in order to extend these synthetic techniques to metals other than platinum which could open up new potential applications.

Appendix A

Interpreting the Electrochemical Voltammetry and Calculation of the Electrochemical Properties

Electrochemistry is a powerful tool which allows for the characterization of catalytic materials. The ECSA is a measure of the active surface area. The mass and specific activities quantify the ability of a catalyst to transport current based on mass and the effective electrochemical surface area. In this report rotating disk electrode cyclic and linear sweep voltammetry were used in order to assure that electrochemical reactions were not diffusion-limited thus providing an accurate relationship between the current density and potential. RDE voltammetry is a standard method for characterization of catalytic materials[64-67].

The ECSA of a material represents the active surface area available for electrocatalytic application. The ECSA value is always lower than the surface area measured by physical adsorption methods such as the Brunauer Emmett Teller (BET) method because physical adsorption does not account for inactive catalytic sites. The ECSA (m^2_{Pt}/g_{Pt}) is calculated from equation A1:

$$ECSA = \frac{Q_H / Q_m}{W} \qquad \text{Equation A1}$$

Where Q_H is the Coulombic charge (C/m^2) normalized for the geometric surface area of the electrode and is determined from a hydrogen adsorption/desorption cyclic voltammogram (CV), Q_m (C/m^2_{Pt}) is the assumed charge density for monolayer adsorption of hydrogen onto an active polycrystalline platinum surface which is generally accepted to be 2.1 C/m^2_{pt} [60] and W (g/m^2) is the platinum catalyst loading on the working electrode. The value of Q_m for monolayer adsorption of hydrogen onto a polycrystalline

platinum surface is justified based on the predominance of the (100) crystal face and is derived as follows[60]. Assuming only one atom of hydrogen adsorbs to one atom of platinum for a monolayer, the number of platinum atoms in a square centimeter of a platinum (100) face (~1.3×10^{15} atoms) is multiplied by $1/N_A$, where N_A is the Avagadro constant (6.022×10^{23} atoms/mole), further multiplied by the Faraday constant (F=96,485 C/mole) and a conversion factor (note: the actual value obtained from calculation is 2.08 C/m^2_{Pt} but is rounded up to account for the presence of other minor crystal planes that might be present).

$$1.3\times10^{15}\,\frac{atoms_{Pt}}{cm^2_{Pt}}\times\frac{mole}{6.022\times10^{23}\,atoms_{Pt}}\times96,485\frac{C}{mole}\times\frac{cm^2}{10^{-4}m^2}\approx2.1\frac{C}{m_{Pt}{}^2}$$

To determine the ECSA we need to obtain a value for Q_H, and for this we employ hydrogen adsorption/desorption cyclic voltammetry. A cyclic voltammogram for the commercial E-TEK platinum black catalyst is shown below in figure A1.

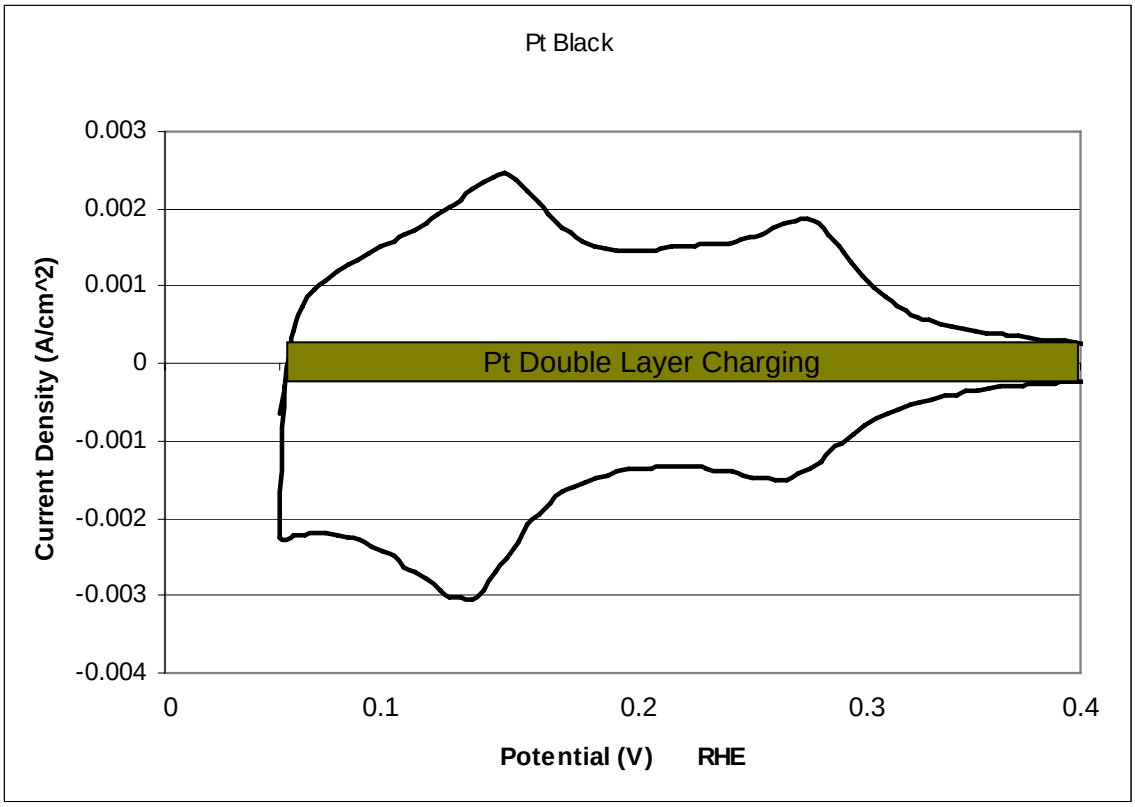

Figure A1: A CV for E-TEK Pt Black with a loading of 0.2 mg_{Pt}/cm^2 showing the hydrogen adsorption/desorption region from 0.05 - 0.4 V and performed using RDE cyclic voltammetry in argon saturated 0.5M H_2SO_4 electrolyte at 1600 RPM's with a sweep rate of 0.05 V/s. The shaded area represents the platinum double layer charging.

Some manipulation of the obtained hydrogen adsorption/desorption CV is necessary to extract the value of Q_H. First, the shaded area is subtracted from the plot to remove any contributions from platinum double layer charging[67]. The platinum double layer charging refers to the capacitance generated at the interface of the first layer of platinum atoms and the electrode surface[67]. Next, the potential axis is converted to a time axis by dividing the potential values by the chosen sweep rate. Two separate values for Q_H are determined from the regions of hydrogen desorption (top half) and adsorption (bottom half). This is accomplished by integrating each half of the plot in the region from 0.05 - 0.4 V with respect to time and taking the absolute values. The trapezoidal rule approximation for the integral was employed in the determination of the values for Q_H. The two values obtained for Q_H from the hydrogen adsorption and desorption regions were averaged and used as Q_H in equation A1 for the all reported ECSA.

Analysis of the oxygen reduction reaction (ORR) yields two important catalytic properties, the mass activity and the specific activity. The mass and specific activities quantify the ability of a catalyst to transport current based on mass and the effective ECSA for a specific mass of platinum respectively. To calculate the values for the mass and specific activity we need to generate a polarization curve using RDE linear-sweep voltammetry. A typical polarization curve for the E-TEK platinum black catalyst is shown in figure A2.

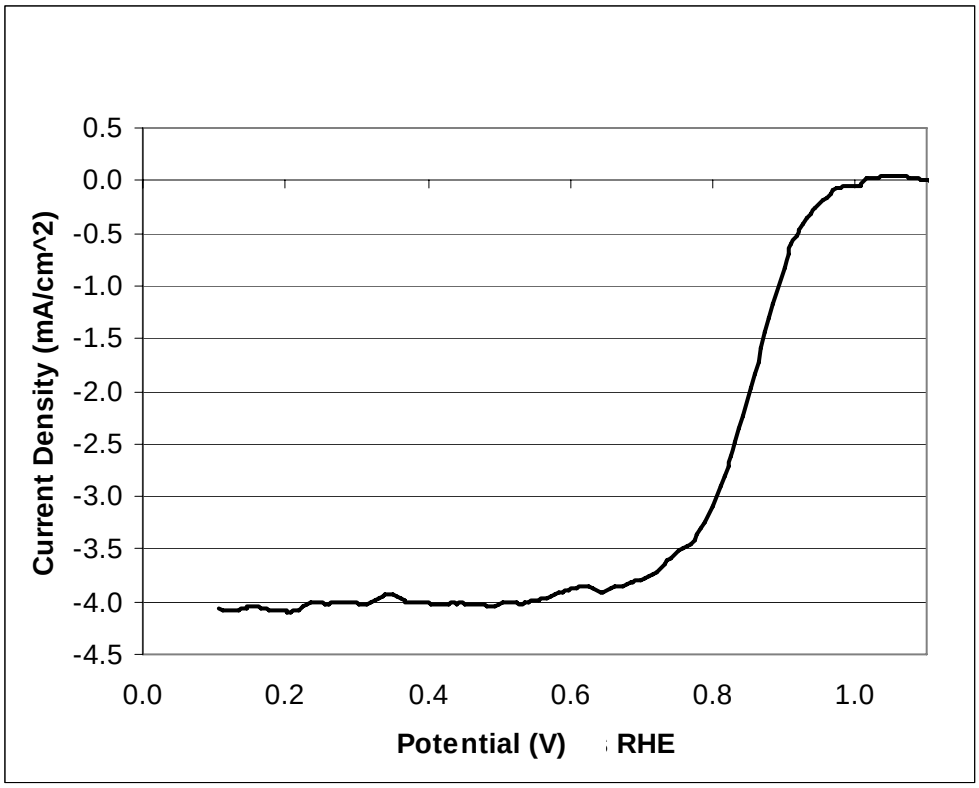

Figure A2: Polarization curve for E-TEK Pt Black obtained by RDE linear sweep voltammetry with a platinum loading of 0.2 mg_{Pt}/cm^2 at 1600 RPMs scanned in the range from 0.05 - 1.1 V RHE in oxygen saturated 0.5 M H_2SO_4 electrolyte and using a sweep rate of 0.005 V/s.

The mass activity can be calculated from equation A2 shown below[61]:

$$A_m = \frac{i_{PolDensity}}{W} \quad \text{Equation A2}$$

Where A_m is the Mass Activity (mA/mg_{Pt}), $i_{PolDensity}$ is the polarization current density normalized for geometric surface area of the electrode at 0.9V and W is the platinum loading (mg/cm^2) on the electrode.

The specific activity is calculated according equation A3 shown below[61]:

$$A_s = \frac{i_{Pol}}{S_r} \quad \text{Equation A3}$$

Where A_s is the specific activity (mA/cm^2_{Pt}), i_{Pol} is the polarization current (not to be confused with the current density) at 0.9V, and S_r is the effective ECSA (cm^2_{Pt}) for the mass of catalyst used.

References

1. Antolini, E., *Mater. Chem. Phys.* **2003,** 78, (3), 563-573.
2. Rolison, D. R., *Science* **2003,** 299, (5613), 1698-1701.
3. Cameron, P. J. P., L. M.; Zakeeruddin, S. M.; Gratzel, M., *Coord. Chem. Rev.* **2004,** 248, 1447-1453.
4. Fang, X. M. M., T. L.; Guan, G. Q.; Akiyama, M.; Abe, E., *J. Photochem. Photobiol. A* **2004,** 164, 179-182.
5. Lim, B. L., X. M.; Jiang, M. J.; Camargo, P. H. C.; Cho, E. C.; Lee, E. P.; Xia, Y. N., *Nano Lett.* **2008,** 8, 4043-4047.
6. Garcia, R. M.; Song, Y. J.; Dorin, R. M.; Wang, H. R.; Li, P.; Qiu, Y.; van Swol, F.; Shelnutt, J. A., *Chem. Commun.* **2008**, 2535-2537.
7. Song, Y. J.; Garcia, R. M.; Dorin, R. M.; Wang, H. R.; Qiu, Y.; Shelnutt, J. A., *Angew. Chem. Int. Ed.* **2006,** 45, (48), 8126-8130.
8. Wang, H., Song, Y., Wang, Z., Medforth, C.J., Evans, L.,Li, P., Shelnutt, J.A., *Chem. Mater.* **2008,** 20, 7434–7439.
9. Chen, J. Y. H., T.; Geissler, M.; Xia, Y. N. , *J. Am. Chem.Soc.* **2004,** 126 10854-10855., 10854-10855.
10. Song, Y., Garcia, R.M., Dorin, R.M, Wang, H., Qiu, Y., Coker, E.N., Steen, W.A., Miller, J.E., Shelnutt, J.A., *Nanoletters* **2007,** 7, (12), 3650-3655.
11. Kijima, T., Yoshimura, T., Uota, M., Ikeda, T., Fujikawa, D., Mouri,; S., U., S., *Angew. Chem., Int. Ed.* **2004,** 43, 228-232.
12. Wu., J. a. L., S., *Adv. Mater.* **2002,** 14, (3), 215-218.
13. Arshak, K., and Mihova, M., *J. Optoelec. and Adv Mater.* **2005,** 7, (1), 193 - 198.
14. Saifullah, M. S. M., Subramanian, K. R. V.,Tapley, E., Kang, D., Welland, M.E, and Butler, M., *Nano Lett.* **2003,** 3, (11), 1587-1591.
15. Jiang, P., Bertone, J. F. and Colvin, V. L. , *Science* **2001,** 291, 453-457.
16. Liang, H. P., Zhang, H. M. , Hu, J. S. , Guo, Y. G. , Wan, L. J. and Bai, C.; L., *Angew. Chem. Int. Ed.* **2004,** 43, 1540.
17. Prodan, E., Radloff, C. , Halas, N. J. and Nordlander, P., *Science* **2003,** 302, 419-422.
18. Sun, Y. G. a. X., Y. N. , *Science* **2002,** 298, 2176-2179.
19. Vasquez, Y., Sra, A. K. and Schaak, R. E. , *J. Am. Chem. Soc.* **2005,** 127, 12504-12505.
20. Wong, M. S., Cha,J. N., ChoiK. S., Deming, T. J. and Stucky, G. D., *Nanoletters* **2002,** 2, (583-587).
21. Song, Y., Garcia, R.M., Dorin, R.M., Wang, H., Qiu, Y., Shelnutt, J.A., *Angew. Chem. Int. Ed.* **2006**, (45), 8126-8130.
22. Song, Y., Dorin, R.M, Garcia, R.M., Jiang, Y., Wang, H., Li, P., Qiu, Y., van Swol, F., Miller, J.E., Shelnutt, J.A., *J. Am. Chem. Soc.* **2008**, (130), 12602-12603.
23. Brinker, C. J., Lu, Y. , Sellinger, A. and Fan, H., *Adv. Mater.* **1999,** 99, (11), 579-585.
24. Y. D. Yin, R. M. R., C. K. Erdonmez, S. Hughes, G. A. Somorjai and A. P. Alivisatos,, *Science* **2004,** 304, 711-714.
25. L. R. Hirsch, J. B. J., A. Lee, N. J. Halas, and J. L. West, *Anal. Chem.* **2003,** 75, 2377–2381.
26. L. R. Hirsch, R. J. S., J. A. Bankson, S. R. Sershen, B. Rivera, R. E. Price, J. D. Hazle, N. J. Halas, and J. L. West, *Proc. Natl. Acad. Sci. U. S. A.* **2003,** 100, 13549-13554.
27. S. Kim, M. K., W. Y. Lee, and T. Hyeon, *J. Am. Chem. Soc.* **2002,** 124, 7642–7643.
28. Y. Xiong, B. W., J. Chen, Z. Li, Y. Yin and Y. Xia, *Angew. Chem. Int. Ed.* **2005,** 44, (48), 79137917.
29. Greenbaum, E., *J. Phys. Chem* **1988,** 92, 4571-4576.
30. Song, Y. J.; Yang, Y.; Medforth, C. J.; Pereira, E.; Singh, A. K.; Xu, H. F.; Jiang, Y. B.; Brinker, C. J.; van Swol, F.; Shelnutt, J. A., *J. Am. Chem. Soc.* **2004,** 126, (2), 635-645.
31. Y. J. Song, Y. B. J., H. R. Wang, D. A. Pena, Y. Qiu, J. E. Miller and J. A. Shelnutt,, *Nanotech.* **2006,** 17, 1300-1308.
32. Wang, Z. L., *Adv. Mater.* **2003,** 15, 1497-1514.

33. Song, Y. J.; Steen, W. A.; Pena, D.; Jiang, Y. B.; Medforth, C. J.; Huo, Q. S.; Pincus, J. L.; Qiu, Y.; Sasaki, D. Y.; Miller, J. E.; Shelnuttt, J. A., *Chem. Mater.* **2006,** 18, (9), 2335-2346.
34. Bittencourt, C. L., E.; Ivanov, P.; Correig, X.; Vilanova, X.; Brezmes, J.; Hubalek, J.; Malysz, K.; Pireaux, J. J.; Calderer, J., *Sens. Actuators B-Chem* **2004**, (97), 67-73.
35. Hrapovic, S. L., Y. L.; Male, K. B.; Luong, J. H. T., *Anal. Chem.* **2004,** 76, 1083-1088.
36. Collins, N. R. T., M. V., *Topics Cataly.* **2007,** 42-43, 323-332.
37. Twigg, M. V., *Catal. Today* **2006,** 117, 407-418.
38. Kordesch, K. V. S., G. R., *Chem. Rev.* **1995**, (95), 191-207.
39. Service, R. F., *Science* **1999**, (285), 682-685.
40. Ginosar, D. M. P., L. M.; Glenn, A. W.; Burch, K. C. , *Int. J. Hydrogen Energy* **2007,** 32, 482-488.
41. Jahagirdar, A. H. D., N. G. , *Sol. Energy Mater. Sol. Cells* **2007,** 91, 1488-1491.
42. Narayanan, R. E.-S., M. A. J., *J. phys. Chem B* **2005,** 109, 12663-12676.
43. Song, Y. J. H., M. A.; Challa, S. R.; Dorin, R. M.; Garcia, R. M.; Wang, H. R.; Jiang, Y. B.; Li, P.; Qiu, Y.; van Swol, F.; Medforth, C. J.; Miller, J. E.; Nwoga, T.; Kawahara, K.; Li, W.; Shelnutt, J. A., *Nano Lett.* **2009**, (9), 1534-1539.
44. Tian, N. Z., Z. Y.; Sun, S. G.; Ding, Y.; Wang, Z. L., *Science* **2007,** 316, 732-735.
45. Sanders, C. R. L., G. C., *Biochemistry* **1995,** 34, 4030-4040.
46. Cui, H. G.; Chen, Z. Y.; Zhong, S.; Wooley, K. L.; Pochan, D. J., *Science* **2007,** 317, (5838), 647-650.
47. Jung, H. T. L., S. Y.; Kaler, E. W.; Coldren, B.; Zasadzinski, J. A. , *Proc. Natl. Acad. Sci. U. S. A.* **2002,** 99, 15318-15322.
48. Waggoner, T. A.; Last, J. A.; Kotula, P. G.; Sasaki, D. Y., *J. Am. Chem. Soc.* **2001,** 123, (3), 496-497.
49. Zemb, T.; Dubois, M.; Deme, B.; Gulik-Krzywicki, T., *Science* **1999,** 283, (5403), 816-819.
50. Marcotte, I.; Auger, M., *Concepts in Magn. Reson. Part A* **2005,** 24, (1), 17-37.
51. Prosser, R. S.; Evanics, F.; Kitevski, J. L.; Al-Abdul-Wahid, M. S., *Biochemistry* **2006,** 45, (28), 8453-8465.
52. Prosser, R. S.; Shiyanovskaya, I. V., *Concepts Magn. Reson.* **2001,** 13, (1), 19-31.
53. Sanders, C. R.; Oxenoid, K., *Biochim. Biophys. Acta* **2000,** 1508, (1-2), 129-145.
54. Sanders, C. R.; Prosser, R. S., *Structure* **1998,** 6, (10), 1227-1234.
55. Song, Y. J.; Dorin, R. M.; Garcia, R. M.; Jiang, Y. B.; Wang, H. R.; Li, P.; Qiu, Y.; van Swol, F.; Miller, J. E.; Shelnutt, J. A., *J. Am. Chem. Soc.* **2008,** 130, 12602-12603.
56. New, R. R. C., *Liposomes: A Practical Approach*. IRL Press: New York: 1989.
57. Mazer, N. A. B., G. B.; Carey, M. C. , *Biochemistry* **1980**, (19), 601-615.
58. Jung, H. T.; Lee, S. Y.; Kaler, E. W.; Coldren, B.; Zasadzinski, J. A., *Proc. Natl. Acad. Sci. USA* **2002,** 99, (24), 15318-15322.
59. Ciacchi, L. C. P., W.; De Vita, A. , *J. Am. Chem. Soc.* **2001,** 123, 7371-7380.
60. Biegler, T., Rand, D.A. J., Woods, R., *J. Electroanal. Chem* **1971,** 29, 269-277.
61. Srinivasan, S., *Fuel Cells: From Fundamentals to Applications*. Springer: 2006.
62. Alam, T., McIntyre, S., *Langmuir* **2008,** 24, 13890–13896.
63. Yu-Min Tsou, L. C., and Emory De Castro, *Prepr. Pap.-Am. Chem. Soc., Div. Fuel Chem.* **2004,** 49, (2), 679-680.
64. Bauer, A., Wilkinson, D. P., Gyenge, E. L., Bizzotto, D., Ye, S., *J. Electrochem. Soc.* **2009,** 156, (10), B1169-B1174.
65. Chen, Z., Waje, M., Li, W., Yan, Y., *Angew. Chem. Int. Ed.* **2007,** 46, 4060-4063.
66. Lim, B., Jiang, M., Camargo, P.H.C, Cho, E.C., Tao, J., Lu, X., Zhu, Y., Xia, Y., *Science* **2009,** 324, 1302-1305.
67. Schmidt, T. J., Gasteiger, H. A., Stab, G. D., Urban, P. M., Kolb, D. M., Behm, R. J., *J. Electrochem. Soc.* **1998,** 145, (7), 2354-2358.